SPARSE SIGNAL RECONSTRUCTION IN LINEAR INVERSE SCATTERING PROBLEM

by

TANMOY BHOWMIK

Presented to the Faculty of the Graduate School of
The University of Texas at Arlington in Partial Fulfillment
of the Requirements
for the Degree of

DOCTOR OF PHILOSOPHY

THE UNIVERSITY OF TEXAS AT ARLINGTON

December 2015

To my parents, wife, son and sister
who set the the inspiration and made me who I am.

ACKNOWLEDGEMENTS

I would like to thank my supervising professor Dr. Soontorn Oraintara for constantly motivating and encouraging me, and also for his invaluable advice and enormous patience during the course of my doctoral studies. I truly appreciate his in-depth knowledge, profound insights and excellent guidance towards research which have led me finish this work. I am grateful to Dr. Hanli Liu who helped me immensely during the last phase of my PhD and guided me in successfully acheiving my research goals. I wish to thank my academic advisors Dr. Kambiz Alavi, Dr. Ioannis D. Schizas and Dr. Michael Manry for their interest in my research and for taking time to serve in my dissertation committee.

I would also like to extend my appreciation to Dr. Fenghua Tian, Dr. Zhou Ye for helping me with the data collection and processing for my research. I wish to thank my friend and fellow student Dr. Jixing Yao for his support and encouragement.

I am grateful to all the teachers who taught me during the years I spent in school, first in India and finally in the Unites States. I would like to thank Dr. Haranath Kar for encouraging and inspiring me to pursue graduate studies. I am indebted to my great teachers including my supervisor, Dr. Alavi, Dr. Schizas, Dr. Hanli Liu and Dr. Yue Liu for making me realize that there is no end of learning.

Finally, I would like to express my deep gratitude to my parents and sister who encouraged and inspired me and always prayed and dreamt for my scholastic achievement. I am extremely fortunate to have my wife stand by me and support me during every phase of my doctoral work while scrificing her own comfort. She has been a continuous source of inspiration and patience during my tough times. My

extended family including uncle, aunts and cousins had always been very supportive and excited about my higher education. And the arrival of my son to this world last year has made the life more beatiful and pushed me to achieve my goal for providing him a better future. I also thank several of my friends, notably Tapangshu Das who have helped me throughout my career in the decision making process.

December 4, 2015

ABSTRACT

SPARSE SIGNAL RECONSTRUCTION IN LINEAR INVERSE SCATTERING PROBLEM

Tanmoy Bhowmik, Ph.D.

The University of Texas at Arlington, 2015

Supervising Professor: Soontorn Oraintara

Proper mathematical modeling of inverse scattering problem is of utmost importance in applications such as optical imaging and microscopy, radar, acoustic, seismic and medical imaging. However, the problem is non-linear and ill-posed due to the diffusive nature of wave propagation through the scattering medium. Born and Rytov approximation are two widely used techniques to linearize the inverse scattering problem that simplifies the mathematics and modeling of wave propagation through scattering medium in special cases. The linear inverse scattering problem is still severely ill-posed and hence, in general, the solution is not stable and unique, unless a priori knowledge about the solution is used to regularize the inverse problem. In many of the inverse scattering problem it is known a priori that the object to be imaged is sparse in spatial domain or in some transform domain. In such cases, regularization techniques that impose sparsity of the solution should be used. The focus of this dissertation is sparsity regularization of the linear inverse scattering problem. The major contributions can be divided in two segments: (*i*) Investigate the condition of uniqueness for the sparsity regularized linear inverse scattering problem and (*ii*)

Propose a dimensionality reduction based optimization method for rapid and high resolution sparse image reconstruction for the inverse scattering problem in optical imaging.

After studying the scattering wave measurement process and the nature of the inverse problem, the condition for obtaining a unique sparsest solution of the linear inverse scattering problem is derived. The condition is based on the degree of sparsity of the image for a fixed source-detector geometry. This result will be useful to determine when one can use Born/Rytov approximation reliably for inverse scattering problem. Computer simulations and laboratory phantom experiments are performed and state-of-the-art sparse signal reconstruction scheme is used to reconstruct the solution. The results show that the quality of reconstruction is satisfactory within the derived sparsity limit.

In the second part of this dissertation, a novel optimization scheme is proposed to solve a particular instance of inverse scattering problem, namely, diffuse optical tomography (DOT), which is a promising low cost and portable imaging modality. Conventional sparse optimization approaches to solve DOT are computationally expensive and have no selection criteria to optimize the regularization parameter. A novel algorithm, Dimensionality Reduction based Optimization for DOT (DRO-DOT), is proposed in this research. It reduces the dimensionality of the inverse DOT problem by reducing the number of unknowns in two steps and thereby makes the overall process fast. First, it constructs a low resolution voxel basis based on the sensing-matrix properties to find an image support. Second, it reconstructs the sparse image inside this support. To compensate for the reduced sensitivity with increasing depth, depth compensation is incorporated in DRO-DOT. An efficient method to optimally select the regularization parameter is developed for obtaining a high-quality DOT image. DRO-DOT is also able to reconstruct high-resolution image even with a

limited number of optodes in a spatially limited imaging set-up which leads towards further application in in-vivo prostate DOT imaging

TABLE OF CONTENTS

Appendix

LIST OF ILLUSTRATIONS

LIST OF TABLES

CHAPTER 1

INTRODUCTION

The problem of determining an object from scattering data has recently received much attention. The task of direct scattering theory is to determine the relation between the medium property and scattered waves, given the details about the scattering target. Inverse scattering theory determines properties of the target, given sufficiently many measurements [1]. How a wave is scattered depends on the difference in constitutive parameters of the inhomogeneity with the reference medium. Inference of properties of such inhomogeneities inside the medium from the detection of scattered waves finds widespread applications in different imaging modalities [2, 3, 4, 5]. In seismic imaging inference is made about the interior structure of the earth by solving the inverse problem of determining the sound speed by measuring travel times of seismic waves. Medical imaging uses scattering of X-rays, ultrasound waves and electromagnetic waves to make images of the human body which is of invaluable help with medical diagnosis. The oil exploration industry uses the reflection of seismic waves in oil prospecting. Inverse scattering is also used in non-destructive evaluation of materials to find cracks and corrosions [1].

In general, scattering from inhomogeneous media is a complex process. The problem is highly nonlinear because of the nonlinear coupling between the unknown medium property and the scattered field [6]. At the same time, due to the diffusive nature of wave propagation and limited number of measurements, the inverse scattering problem is severely ill-posed. Because of the difficulty of modeling arbitrary inhomogeneous scatterers, approximations are frequently made that simplify the mathematics and modeling in special cases [7]. The conventional inversion approach to deal with nonlinearity is linearization, i.e., to approximate the measurement as a linear function of the perturbation in medium property [8]. The two most commonly used linearization approaches are Born and Rytov approximation. Born approximation assumes that the scattered field is proportional to the variation in medium property, while Rytov approximation linearizes the scattered phase with respect to perturbation in medium property [8]. The linear inverse problem is still ill-posed which results in non-uniqueness and instability of the solution. However, in many of the inverse scattering problems this ill-posedness is overcome by using a priori knowledge of the solution. This technique of incorporating prior knowledge such as smoothness, bounded variation, sparsity, of the underlying image in the inverse problem formulation is called regularization [9, 10, 11]. Different optimization schemes can be adopted to reach the solution of different regularized linear inverse scattering problems (LISP)[4, 12, 13].

1.1 Unique Sparse Recovery

In many of the LISPs such as medical imaging, the inhomogenious object is localized occupying only a small portion of the whole field of view, which implies that the underlying image representing medium property variation is sparse [14]. By exploiting this additional sparsity constraint it is possible to find the unique and stable solution for the ill-posed LISP [15]. The problem of sparse signal recovery is well studied in the area of compressed sensing [16, 17]. It is provable that having sparsity below some bound is a sufficient condition for the solution to be the unique sparsest one [18]. In the first part of this thesis, the goal is to derive the sparsity bound for the uniqueness of inverse scattering solution using Born and Rytov approximation. The approach is based on the finding that Born and Rytov approximation can be reformulated as particular instances of multiple measurement vector (MMV) problem. Computer simulation and laboratory phantom experiments are used to validate the unique sparse recovery condition.

1.2 Dimensionality Reduced Optimization

The second part of the thesis contributes towards developing a computationally efficient optimization method for solving an instance of LISP arising in the field of medical imaging, called diffuse optical tomography (DOT). State of the art ℓ_1 norm minimization techniques involves solving a linear system with the size of the unknown image which ensues a huge computational burden for the full 3-D imaging volume [19, 20]. Hence the current sparse optimization approaches are not suitable or practical for 3-D DOT reconstruction in real time.

A major challenge for the researchers in solving regularized inverse problem is to select the correct regularization parameter. For sparsity enhanced optimization, choosing the regularization parameter is still an unsolved technical problem and the choice is made empirically [21, 12, 22].

The second challenge in DOT is that DOT reconstruction suffers from poor depth localization as the sensitivity of DOT measurement decreases exponentially along the depth [23, 24]. Pogue et al. proposed a spatially variant regularization scheme to enhance depth sensitivity [25]. Recently a more direct approach of modifying the sensing matrix to compensate for sensitivity decrease with increasing depth has been adopted [24, 26].

Another challenge for DOT research community is the optode geometry optimization, with which high quality reconstruction can be obtained by deploying a minimum number of optodes. Tian et al. have studied different optode configurations to find the optimal measurement density using ℓ_2-based regularization [27].

This dissertation demonstrates a novel reconstruction method that is able to overcome the challenges mentioned so far for solving the sparse DOT inverse problem. For sparse images, the size of the linear system for the inverse problem can be reduced drastically if one can approximately create a low-resolution support mask of the nonzero voxels beforehand. Motivated by this insight, a two-step, dimensionality-reduction-based optimization (DRO) algorithm for DOT image reconstruction has been developed. In the first step, DRO-DOT finds a low resolution support mask of the sparse image to be reconstructed by identifying and grouping the sensing columns of the measurement or sensing matrix and the corresponding image voxels. The number of such groups is far less than the number of original voxels. In the second and final step, sparse optimization is carried inside the recovered support mask only, whose size is smaller than the full 3-D imaging volume. Hence in both steps the number of unknowns is reduced, resulting from dimensionality reduction of the original problem and thereby scaling down the computational complexity. In addition, the sensing matrix is re-weighted to enhance the depth sensitivity of the overall method by including depth compensation. The critical problem of chosing the regularization parameter is also addressed by developing an adaptive scheme to find the parameter based on the statistical interpretation of sprasity regularization. It will be shown that DRO-DOT is able to recover high-resolution images even with a limited number of optodes, which in turn reveals the possibility and feasibility of using transcretal DOT for prostate cancer imaging.

Overall, the major novelty of this approach is to solve an optimization model that consists of a data residue item and a sparse regularization item. The algorithm leads to three advantages: (1) It forms a low resolution supporting basis to reduce computional complexity. (2) It refines the depth compensation algorithm so as to recover more accurate DOT images. (3) It offers a semi-automatic method to choose optimal regularization parameter.

1.3 Thesis outline

Chapter 2 provides a brief review of the background study related to Born and Rytov approximation and inverse problem. In chapter 3 the condition for sparse image reconstruction under both Born and Rytov approximation is presented and the simulation and experimental results to test the sparse recovery condition are shown. Chapter 4 presents a dimensionality reduced two step inverse scattering solver for rapid and high quality DOT image reconstruction . Laboratory phantom experiments are carried out to quantify the speed and performance of the algorithm. Summary and possible future directions are discussed and listed in chapter 5.

CHAPTER 2

LINEAR INVERSE SCATTERING PROBLEM

Modeling the propagation and scattering of waves in inhomogeneous media is necessary to solve both the direct and inverse scattering problems. Given an accurate or approximate model of the scattering phenomenon for the particular application, inverse scattering problem extracts the properties of inhomogeneity inside the scattering media from the measurable quantities such as the scattered fields and intensities [7].

2.1 Lineariation of scattering problem

Usually, approximations are sought in order to linearize the model of scattering wave propagation inside inhomogenious media and thus making it more tractable for numerical computation. Two first-order approximations being most commonly exploited are the Born and the Rytov linear methods. For the Born approximation, the scattered field is modeled as a linear function of the medium object function representing the change in medium properties inside the heterogeneity from the background homogenious medium. On the other hand, in Rytov approximation linear relation between the scattered phase and object function is assumed [7]. Here the focus is on the continuous wave (CW) measurement i.e. wave with zero modulation frequency.

2.1.1 Born Approximation

For Born approximation, the total fluence or total field $U(r)$ is expressed as [28]:

$$U(r) = U_0(r) + U_{sc}(r),$$

where $U_0(r)$ is the incident field that would have been detected if no heterogeneity was present i.e. for homogenious medium, and $U_{sc}(r)$ is the scattered field which is only due to the perturbation of medium property inside heterogeneity. The Born approximation produces a linear relation between the monochromatic scattered wavefield U_{sc} and a perturbed velocity field expressed as the object function O [5]:

$$U_{sc}(d, s) = -\int_{\Omega} g(r, d) U_0(s, r) O(r) dr, \tag{2.1}$$

under the assumption that $U_0(r) >> U_{sc}(r)$. g is the Green's function given by,

$$g(x, y) = \frac{exp(-K|x-y|)}{4\pi|x-y|}, \tag{2.2}$$

with K being the wavenumber. Ω denotes the imaging volume and $U_{sc}(d, s)$ stands for the scattered field at detector position d due to source placed at s. Once the space is discretized into n equally spaced voxels located at $\{r_k\}_{k=1}^{n}$, the scattered field $U_{sc}(d, s)$ in (2.1) can be approximated by

$$U_{sc}(d, s) \approx -\sum_{k=1}^{n} g(r_k, d) U_0(s, r_k) O(r) h^3,$$

where h^3 is the volume of each voxel. Let there be q sources and m detectors located at $\{s_i\}_{i=1}^{q}$ and $\{d_i\}_{i=1}^{m}$ respectively. So there will be a total of $m \times q$ measurements if one takes a measurement for every source-detector pair. Hence the linear equation for Born approximation becomes:

$$y^B = A^B x, \tag{2.3}$$

where $y^B = [y^B(d_1, s_1), \ldots, y^B(d_m, s_q)]^T$ is the measurement vector, $x = [O(r_1), O(r_2), \ldots, O(r_n)]^T$ is the image vector representing the object function and A^B is the Born sensing matrix given by:

$$A^B = \begin{bmatrix} A^B_{(1,1),1} & . \quad . & A^B_{(1,1),n} \\ . & & . \\ A^B_{(m,1),1} & & A^B_{(m,1),n} \\ . & . & . \\ . & . & . \\ A^B_{(m,q),1} & . \quad . & A^B_{(m,q),n} \end{bmatrix}. \tag{2.4}$$

Here $y^B \in R^{mq\times 1}$, $x \in R^{n\times 1}$ and $A^B \in R^{mq\times n}$. The elements of A^B determine the weight of each voxel in every measurement. Thus the sensitivity of the voxel k in the measurement at the detector d_i due to the source s_j is given by

$$A^B_{(i,j),k} = -g(r_k, d_i)U_0(s_j, r_k)\, h^3. \tag{2.5}$$

2.1.2 Rytov Approximation

The Rytov approximation expresses the total fluence or total field $U(r)$ in terms of homogenious $(\phi_0(r))$ and scattered heterogenious $(\phi_{sc}(r))$ complex phases [28]:

$$U(r) = exp(\phi_0(r) + \phi_{sc}(r)),$$

where the incident field is $U_0(r) = exp(\phi_0(r))$. Hence the scattered phase is measured as

$$\phi_{sc}(r) = \ln\left(\frac{U(r)}{U_0(r)}\right).$$

Rytov approximation produces a linear relation between the monochormatic scattered phase ϕ_{sc} and object function O. The scattered phase at the detector position r_d due to the source placed at r_s can be expressed by [29]:

$$\phi_{sc}(d, s) = \frac{-1}{U_0(d, s)} \int_{\Omega} g(r, d) U_0(s, r) O(r) dr. \tag{2.6}$$

under the assumption that the scattered phase is slowly varying spatially ($\nabla \phi_{sc}(r) << O(r)$). Using the same measurement geometry with n voxels, q sources and m detectors discussed in the previous section, the discrete linear equation for Rytov approximation becomes:

$$y^R = A^R x, \tag{2.7}$$

where $y^R = [y^R(d_1, s_1), \ldots, y^R(d_m, s_q)]^T$ is the measurement vector and x is the same image vector as described earlier. The Rytov sensing matrix A^R is given by:

$$A^R = \begin{bmatrix} A^R_{(1,1),1} & & A^R_{(1,1),n} \\ \cdot & & \cdot \\ A^R_{(m,1),1} & & A^R_{(m,1),n} \\ \cdot & \cdot & \cdot \\ \cdot & \cdot & \cdot \\ A^R_{(m,q),1} & & A^R_{(m,q),n} \end{bmatrix}, \tag{2.8}$$

where

$$A^R_{(i,j),k} = -\frac{g(r_k, d_i) U_0(s_j, r_k)\, h^3}{U_0(d_i, s_j)}. \tag{2.9}$$

is the weight for the voxel k in the measurement at the detector d_i due to the source s_j.

2.2 Inverse Problem

The general linear scattering problem takes the form,

$$y = Ax + e, \tag{2.10}$$

where y is either the Born or Rytov measurement, A is either the Born or Rytov matrix and e is the measurement noise. Due to the limited numbers of sources and detectors, the number of measurements obtained is much fewer than that of the voxels in x to be reconstructed. As a result, the **A** matrix is highly ill-posed and the solution is non-unique and unstable [**?**]. Hence, it is obvious that to find the correct solution, one needs some a priori information about x. The technique of using such a priori knowledge to restrict the solution space is termed as regularization.

In many of the applications, it is known a priori that the object function representing the heterogeneous perturbation is localized in some small volumes inside the medium or it can be represented by a few number of transform coefficients in some transform domain. This in turn implies that x is sparse [14] spatially or in some transform domain. Therefore, sparsity based regularization techniques that restrict the number of nonzero elements in the solution demands attention.

2.2.1 Sparsity Regularization

Given the linearized Born and Rytov forward models in (2.3) and (2.7), the inverse problem of finding the unique sparsest solution essentially becomes solving the optimization problem [30] :

$$(P0) \;\; \text{minimize} \, ||x||_0 \;\; \text{subject to} \;\; y = Ax,$$

where $|| \, ||_0$ stands for the sparsity or ℓ_0 norm which is same as the number of nonzero elements of the vector. This is equivalent to solving 4.15 assuming the linear approximation to be exact in absence of noise, i.e., for $e = 0$. Now the question is, under what condition one can obtain a unique solution of $(P0)$. Donoho et. al. have proved that if x is sparse enough such that $||x||_0 < \frac{spark(A)}{2}$ [31] then this is necessarily the sparsest possible solution of (4.15). The spark of a matrix is defined as follows,

Spark : Given a matrix A, $p = spark(A)$ is defined to be the smallest possible number p, such that there exists a sub-groub of p columns from A that are linearly dependent, which means any sub-group of (p-1) columns are linearly independent.

Thus having sparsity of x less than $spark(A)/2$ ensures that it is the unique sparsest representation and therefore the unique solution of $(P0)$. It is straightforward to show that $2 \leq spark(A) \leq rank(A) + 1$. But finding the spark of a matrix is a combinatorially hard problem to solve [30]. Typically the number of measurements $m \times q$ is less than the number of voxels n in the imaging domain. Hence $rank(A) \leq m \times q$. As the structure of matrix A solely depends on the source-detector positions, one may think that by optimizing the source-detector geometry one can achieve the best case scenario $spark(A) = (rank(A) + 1) = (m \times q + 1)$ i.e. to make any $m \times q$ set of columns of matrix A independent and hence guarantee the uniqueness of the linear inverse scattering problem upto a maximum sprasity level $\frac{m \times q}{2}$. Indeed, this is not achievable as it will be shown that the allowable sparsity bound is of the order of total number of sources and detectors instead of being of the order of their product. This result is very important as it imposes a limit on the degree of sparsity of the solution for the inverse Born/Rytov problem. The derivation of this result is based on the observation that the single measurement vector formulation for Born (2.3) and Rytov (2.7) approximation can be reformulated as multiple measurement vector (MMV) problem. The uniqueness condition for the sparse solution of such MMV problem has already been found by Chen and Huo [18] and Davis and Eldar [15].

CHAPTER 3

UNIQUE SPARSE RECOVERY

To derive the uniqueness condition, the first step will be to show that the Born/Rytov approximation in (2.3)/ (2.7) can be reformulated as an MMV problem of the form $Y^* = GZ$ where $Y^* \in R^{m\times q}$, $G \in R^{m\times n}$ and $Z \in R^{n\times q}$ such that the nonzero rows of Z corresponds to the nonzero element of x. In that case if the row diversity measure i.e. the number of nonzero rows of Z is defined as $||Z||_0$, then $||Z||_0 = ||x||_0$. Here the i^{th} column of the measurement matrix $Y^* \in R^{m\times q}$ relates to the i^{th} snapshot, i.e. measurements at all the detectors for the i^{th} source. Thus an MMV optimization problem equivalent to $(P0)$ is obtained as:

$$(P0_{MMV}) \quad \text{minimize}\, ||Z||_0 \;\text{ subject to }\; Y^* = GZ.$$

Chen and Huo provided the sufficient condition for the uniqueness of $(P0_{MMV})$. Recently, Davies and Eldar showed that the sufficient condition is also indeed necessary.

Theorem 1: Chen and Huo [18], Davies and Eldar [15]: Let rank(Z) denotes the rank of the matrix Z, then $(P0_{MMV})$ has a unique solution if and only if

$$||Z||_0 \leq (spark(G) + rank(Y^*) - 1)/2. \tag{3.1}$$

Theorem 1 will be used to find the sparsity bound for uniqueness of Born/Rytov linear inverse scattering problem in the subsequent sections.

3.1 Uniqueness for Born Approximation

The Born approximation in (2.3) can be converted into a multiple measurement vector (MMV) problem as follows :

$$Y^{B*} = GZ, \tag{3.2}$$

where the matrix Y^{B*}, G and Z are defined as follows :

$$Y^{B*} = \begin{bmatrix} y^B(d_1, s_1) & & y^B(d_1, s_q) \\ \vdots & \ddots & \vdots \\ y^B(d_m, s_1) & & y^B(d_m, s_q) \end{bmatrix} \in R^{m \times q}, \tag{3.3}$$

$$G = \begin{bmatrix} g(d_1, r_1) & & g(d_1, r_n) \\ \vdots & \ddots & \vdots \\ g(d_m, r_1) & & g(d_m, r_n) \end{bmatrix} \in R^{m \times n}, \tag{3.4}$$

$$Z = \begin{bmatrix} U_0(s_1, r_1)x(1) & & U_0(s_q, r_1)x(1) \\ \vdots & \ddots & \vdots \\ U_0(s_1, r_n)x(n) & & U_0(s_q, r_n)x(n) \end{bmatrix} \in R^{n \times q}. \tag{3.5}$$

Clearly the nonzero rows of Z correspond to the nonzero elements of x i.e. $||Z||_0 = ||x||_0$. Hence by converting equation (2.3) into an equivalent MMV problem as in (3.2), the $(P0)$ problem can be reformulated to find a unique sparse solution for the Born approximation case as follows,

$$(P0\_Born_{MMV}) \quad \text{minimize} \, ||Z||_0 \quad \text{subject to} \quad Y^{B*} = GZ.$$

From Theorem 1 it follows:

$$||Z||_0 \leq (spark(G) + rank(Y^{B*}) - 1)/2. \tag{3.6}$$

Theorem 1 provides insight into the ultimate number of targets that the linear inverse Born problem can recover. Since $rank(Y^{B*}) \leq q$ and $spark(G) \leq m + 1$, the maximum number of targets that can be recovered is given by

$$||x||_0 = ||V||_0 \leq (m + q)/2, \tag{3.7}$$

which corresponds to the average of the numbers of the source and detector elements. Here while stating $rank(Y^{B*}) \leq q$, it is assumed that the number of detectors is more than the number of sources, which is true for typical inverse scattering problems such as optical tomography [14] and seismic imaging [32].

3.2 Uniqueness for Rytov Approximation

The uniqueness result for Born approximation also follows for Rytov approximation because the columns of the Rytov matrix are nothing but weighted columns of the Born matrix A^B. So the linear dependency among the columns of A^R remains unchanged. Specifically from (2.4), (2.5),(2.8) and (2.9), one can write:

$$A^R = diag(M)\, A^B,$$

$$\text{where } M = \begin{bmatrix} U_0(d_1, s_1) \\ . \\ . \\ U_0(d_m, s_1) \\ . \\ . \\ . \\ U_0(d_m, s_q) \end{bmatrix} \in R^{mq \times 1}.$$

Hence (2.7) can be re-written as

$$y^R = diag(M)\, A^B x. \tag{3.8}$$

Following the discussion in the previous section of MMV formulation in the Born case, the above equation is equivalent to the MMV form:

$$Y^{R*} = GZ, \tag{3.9}$$

where the matrix Y^{R*} is defined as

$$Y^{R*} = \begin{bmatrix} y^R(d_1, s_1)U_0(d_1, s_1) & & y^R(d_1, s_q)U_0(d_1, s_q) \\ \vdots & \ddots & \vdots \\ y^R(d_m, s_1)U_0(d_m, s_j) & & y^R(d_m, s_q)U_0(d_m, s_q) \end{bmatrix} \in R^{m \times q}. \tag{3.10}$$

Thus the $(P0)$ problem for Rytov approximation is now formulated as:

$$(P0\_Rytov_{MMV}) \qquad \text{minimize } ||Z||_0 \qquad \text{subject to} \qquad Y^{R*} = GZ.$$

Due to Theorem 1 $(P0\_Rytov_{MMV})$ has unique solution if and only if,

$$||Z||_0 \leq (spark(G) + rank(Y^{R*}) - 1)/2. \tag{3.11}$$

Again by assuming $rank(Y^{R*}) \leq q$, and hence the maximum number of target that can be recovered uniquely is given by

$$||x||_0 = ||Z||_0 \leq (m + q)/2. \tag{3.12}$$

Note that the sparsity bound for both Born and Rytov case is found because the linear approximation can be converted into the MMV form. This MMV formulation comes from the finding that it is possible to decouple the source to voxel and voxel to detector scattering terms in the Born and Rytov formulation seperately in the G and Z matrices. Otherwise finding the uniqueness condition would have been an NP - hard problem to solve.

3.3 Verification Issues

In general, finding ℓ_0 norm based solutions for $(P0)$ requires enumerating subsets of the columns of the sensing matrix looking for the smallest subset able to represent the image. The complexity of such subset search grows exponentially with n [31]. So $(P0)$ is combinatorially hard to solve. Also, the uniqueness condition has been derived for noiseless case. It is warranted to verify if the uniqueness condition is relevant in presence of noise for actual measurement data.

3.3.1 ℓ_1 relaxation of $(P0)$

As stated, $(P0)$ seems to be a general combinatorial optimization problem, requiring that one enumerates all possible k-element collections of columns of A, for k = 1, 2, . . . ,n, looking for the smallest collection permitting representation of the signal. Such an algorithm would cost at least $O(2^m)$ flops to carry out in general. It is, therefore, desirable to turn into approximations/relaxations of $(P0)$. A formal approach is to convexify $(P0)$ by replacing the ℓ_0-norm with the ℓ_1-norm:

$$(P1) \quad \text{minimize} \, ||x||_1 \quad \text{subject to} \quad y = Ax.$$

The ℓ_1 norm acts as the sparsity inducing regularizer. This approach to sparse signal representation is called Basis-Pursuit (BP) in [30], which observed that it gave highly sparse solutions to problems known to have such sparse solutions. The key point about BP is that it is much more practical than direct solution of $(P0)$ and in most of the cases, correctly solves $(P0)$. Thus, $(P1)$ can find the sparse solution of $(P0)$ that otherwise on the surface seem computationally intractable. The detail of $(P0)$ - $(P1)$ equivalence will not be discussed here as it is out of the scope of this work. Henceforth, due to its tractability and sparsity enforcing behaviour, minimization of the ℓ_1 norm will be carried out instead of ℓ_0 norm to find the sparse solution of LISP and verify the uniqueness condition.

3.3.2 Noise and Approximation error

Though the derivation of the uniqueness condition is for noiseless case, it will be interesting to analyze the sparse recovery result for real noisy measurements described by equation , under and above the uniqueness bound. For this the inequality constrained optimization problem ($P1_{denoise}$) is defined as:

$$(P1_{denoise}) \quad \text{minimize} \; ||x||_1 \quad \text{subject to} \quad ||y - Ax||_2^2 < \epsilon$$

where it is assumed that e is zero mean gaussian i.i.d. with variance ϵ [31]. This formulation is known as basis pursuit denoising (BPDN) in standard compressive sensing literature [13].

Using the Lagrangian of the equality constrained ($P1$) or the inequality constrained ($P1_{denoise}$) optimization problem, the general unconstrained optimization problem ($Q1$) can be obtained:

$$(Q1) \quad \text{minimize} \; ||Ax - y||_2^2 + \lambda ||x||_1,$$

where, $\lambda(x, \epsilon)$ is the regularization parameter/Lagrangian multiplier which depends on the noise level and solution sparsity [16]. By solving ($Q1$) with appropriate λ, it is possible to find the sparsest solution of the LISP. It is also termed as penalized least square problem, as the solution norm is penalized while fitting the solution to the measurement using least square approach. Split Augmented Lagrangian Shrinkage Algorithm (SALSA) is used for solving ($Q1$) as it is currently known to be the fastest state of the art algorithms for penalized least-square problem [19].

3.4 Experimental Results

In this section the uniqueness condition derived for Born/Rytov approximation based inverse scattering problem will be validated by experimental studies. The focus is on one particular application of inverse scattering problem in the area of diffuse optical tomography (DOT). DOT is a non-invasive and low-cost imaging modality which reconstructs optical properties of highly scattering medium in the near infra red (NIR) domain from the measurement of scattered and attenuated optical flux at the surface of the imaging volume. As the absorption of light in human tissues is low in the NIR region, so NIR photons can penetrate several centimeters inside the tissue [33]. This makes DOT a promising tool in several biomedical imaging applications such as brain imaging, breast cancer detection and molecular imaging etc. For DOT the object function $O(r)$ is a linear function of tissue absorption perturbation $\Delta\mu_a(r)$ assuming that the scattering coefficient is nearly constant in the tissue which is typically valid for human issues [14]. For details about how a DOT reconstruction problem is formulated as an inverse scattering problem, the interested readers are encouraged to refer to the excellent literature on this topic [4, 5, 29]. Similar to other inverse scattering problems, Born and Rytov approximation has been extensively used to linearize the DOT inverse problem. Hence it is required to experimentally validate the uniqueness condition derived in the last two sections for the DOT problem.

In the first experiment the measurement data are generated by using the Born/Rytov approximation for a 2D DOT problem. The matrix A^B/A^R is generated by the PMI toolbox [34] for a fixed source detector geometry and 2-D imaging area. This corresponds to the ideal linear and noiseless scenario where it is explicitly assumed that the measurements do not differ from approximation due to nonlinearity or noise. For this case one should get unique solution below the sparsity bound and should expect non-uniqueness resulting in possible error in reconstruction as the bound is violated.

In the second experiment, the measurements are generated by solving the nonlinear forward scattering problem or the diffusion equation using finite element method. The TOAST toolbox [35] has been used to implement the finite element model (FEM). The inverse problem is linearized using both Born and Rytov model and again the reconstruction error below and above the sparsity bound is examined.

A real phantom experiment is performed at the end to get the real DOT measurement data and the reconstruction performance is evaluated below and above the uniqueness bound.

Before elaborating on each of these experiments, it is worth to mention about few assumptions and experimental set-up which are common for all the three experiments.

1. The geometry of the sources and detectors is illustrated in Fig. 3.1, where 12 sources and 13 detectors (156 measurements) are placed in a 6×6 square grid over the top surface of a 6 cm deep slab medium. The distance between every two closest optodes is 1.4 cm. The absorption and reduced scattering coefficients of the homogeneous background medium are chosen in a reasonable range for human tissue [36] as $\mu_{a_0} = 0.06$ cm^{-1} and $\mu_{s_0} = 8.2$ cm^{-1} respectively, in all the experiments. The image plane is located at a depth of 2 cm.
2. As given by equation (3.7) / (3.12), the maximum sparsity bound is the average number of sources and detectors. Hence in this paper sparse reconstruction performance below and above this bound ($\frac{m+q}{2}$) will be analyzed. A similar study has been done in MMV-based DOT reconstruction problem in [14], but it did not cover Born or Rytov approximation.

3.4.1 Numerical Validation

In order to verify the sparse recovery condition for Born/Rytov approximation just derived above, a numerical experiment is carried out. In the experiment the Born (Rytov) matrix $A^B(A^R)$ is generated for the given source detector geometry and 32 by 32 voxel image. The forward data is generated as $y = Ax$ where A is the

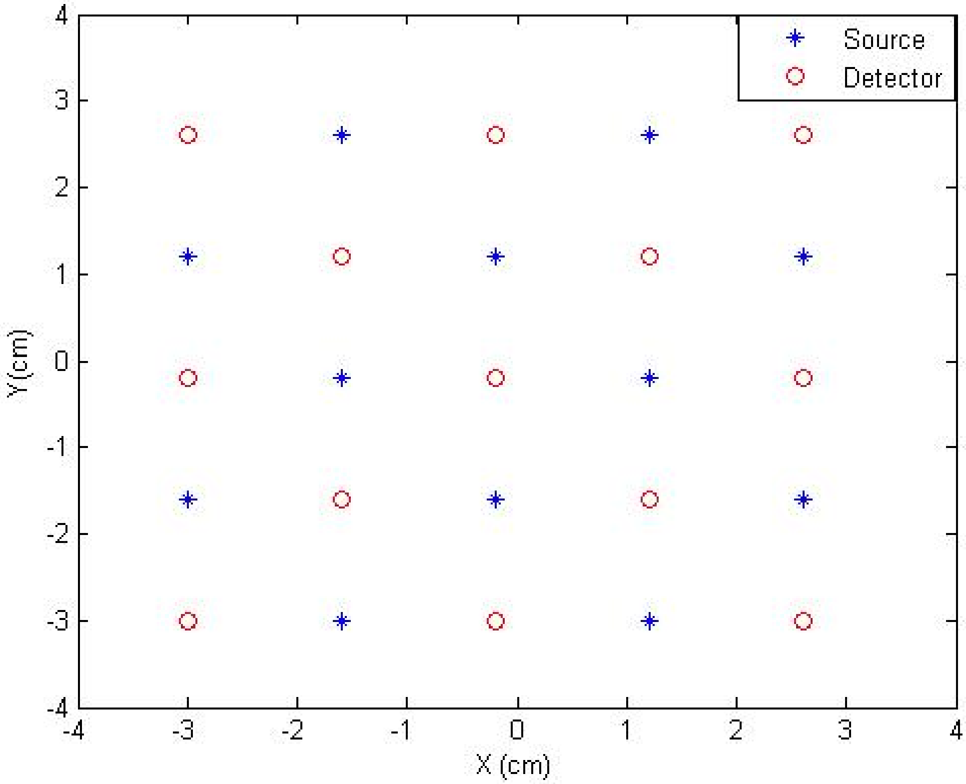

Figure 3.1. Optode configuration for both Simulation and Phantom experiment.

Born (Rytov) matrix $A^B(A^R)$ and x is the sparse object with a sparsity level ($||x||_0$) ranging from 1 to 25. The locations of the nonzero voxels are choosen randomly. According to the finding in this paper the sparsity bound should be 12 ($[\frac{12+13}{2}]$) for uniqueness of the sparse solution. For each sparsity level from 1 to 25, every time 100 simulations are run. In each simulation the nonzero voxel locations are randomly choosen and the $(P1)$ problem is solved using SPGL1 Basis Pursuit solver [37] with random initialization. From these simulations the empirical probability of perfect reconstruction is calculated for each sparsity level. The probability of correct sparse recovery for Born and Rytov case is shown in Fig. 3.2. From the figure it is observed that below the sufficient sparsity level, which in this case is 12 , perfect reconstruction

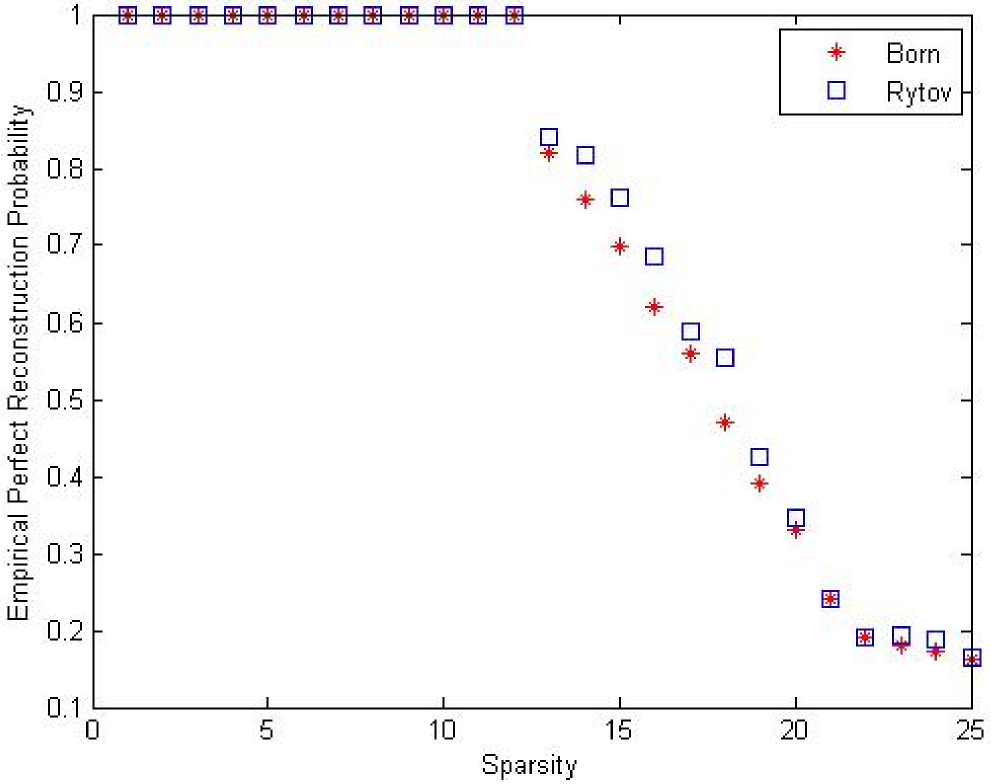

Figure 3.2. Empirical probability of perfect reconstruction with different sparsity levels for the noiseless case of Born and Rytov based inverse DOT problem.

is achieved for both Born and Rytov approximation. When $||x||_0$ increases beyond the sparsity bound, the probability of of perfect reconstruction gradually decreases, implying that the sparsest reconstruction is no more the same as original image.

3.4.2 Simulation Experiment

Next, the validity of the sparse reconstruction condition is checked with a computer simulation. In the simulation a continuous wave DOT system is considered and the forward data is generated by solving the direct scattering problem numerically. Born and Rytov model is used for image reconstruction. Hence this paper is necessarily analyzing the reconstruction performance below and beyond the sparsity bound in presence of approximation error. The direct scattering problem or the diffusion equation is solved by finite element method. The TOAST toolbox [35] has been used to implement the finite element model (FEM).

Simulations are run for different levels of sparsity of the absorption heterogeneity ranging from 0 to 50. $\Delta\mu_a$ is assumed to be 0.06 cm^{-1} for each level of sparsity. The reconstruction is run for both Born and Rytov approximation with the FEM measurements. For each level of sparsity of x, $(Q1)$ is solved with different value of λ(giving different sparse solution) and keep the sparsest solution satisfying $||Ax - y||_2^2 < \epsilon$ where ϵ is the squared norm of the approximation error.

Fig. 3.3 shows the original images and the reconstructed images using Born and Rytov approximation for various levels of sparsity. It is found that that below the sparsity bound the reconstructed and original image has same sparsity, though they differ in magnitude which is beacause of the approximation error. But beyond the sparsity bound, the solution sparsity becomes less than the sparsity of the original image. Fig. 3.4 shows the normalized reconstruction error for Born and Rytov approximation with respect to sparsity level. The plots show that if the sparsity of the underlying image is within the sufficient sparsity bound, then Born/Rytov approximation based inverse problem formulation gives reasonable reconstruction performance. Also as the size of the heterogeneity, i.e. sparsity, increases, Rytov gives better reconstruction performance than Born approximation. This is because of the fact that Born approximation breaks down when the size of the absorption heterogeneity becomes relatively large compared to the background, whereas Rytov approximation is still valid for large size of heterogeneity [5].

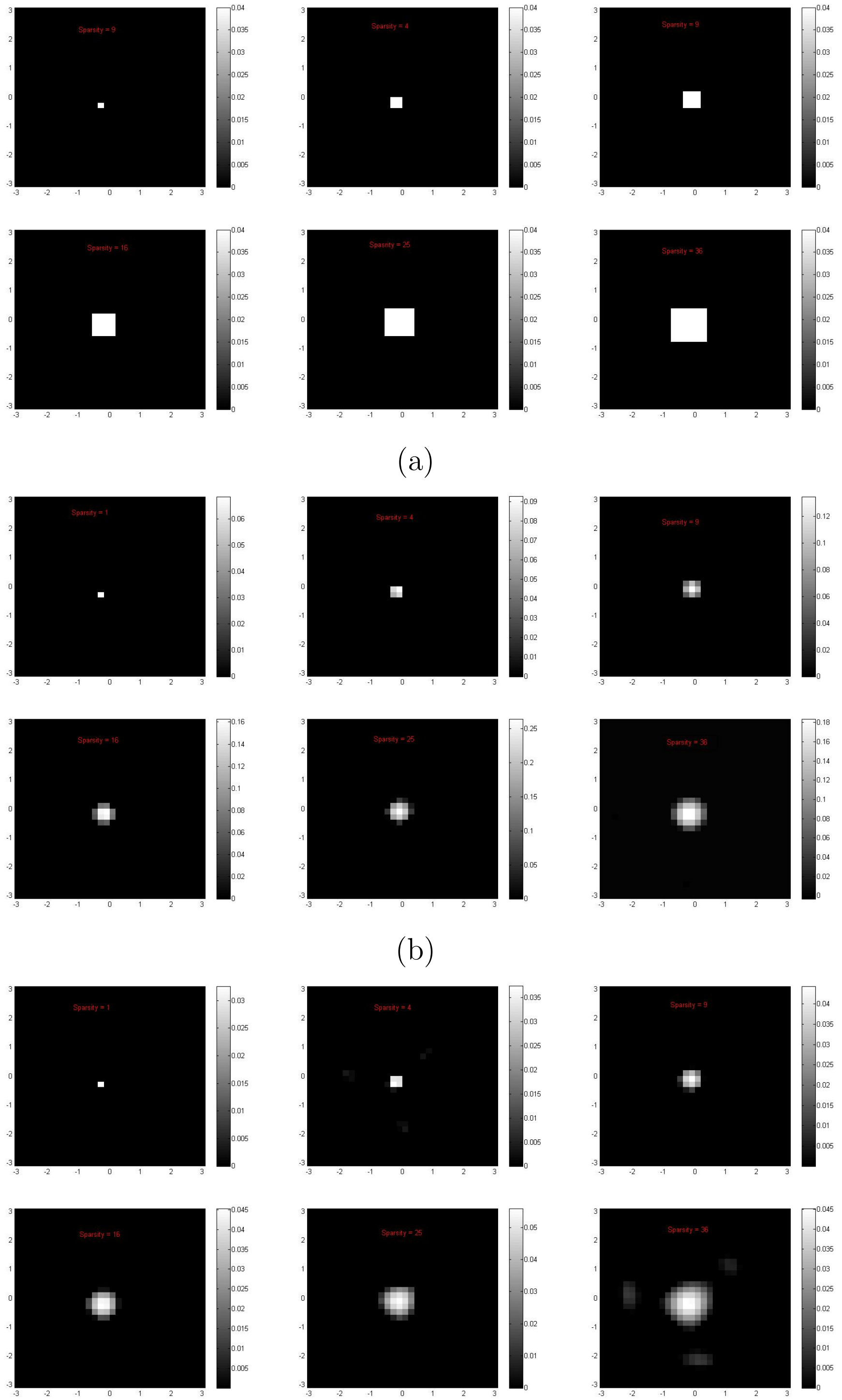

(a)

(b)

(c)

Figure 3.3. Reconstruction with different sparsity level (1, 4, 9, 16, 25 and 36) using forward FEM simulated data (a) Original Image; (b) Reconstruction using Born Approximation; (c) Reconstruction using Rytov Approximation.

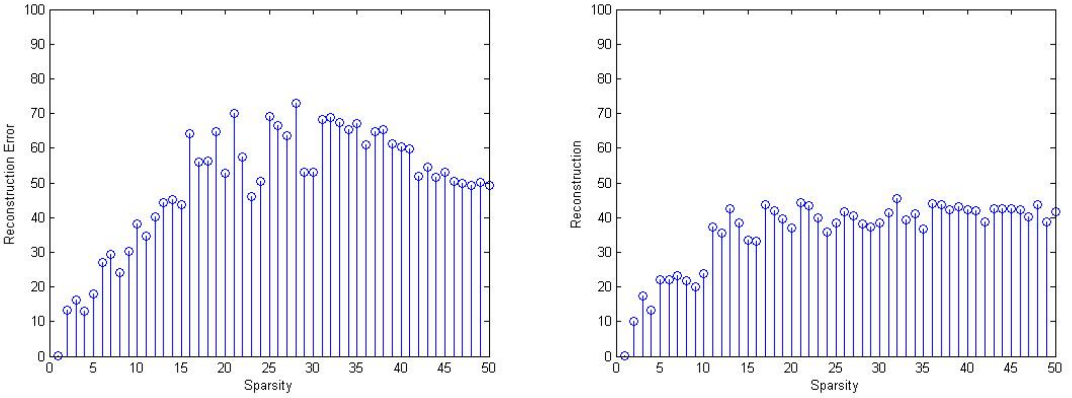

(a) (b)

Figure 3.4. Sparsity level vs normalized reconstruction error using forward FEM simulated data for (a) Born; (b) Rytov method.

3.4.3 Phantom Experiment

A laboratory phantom experiment is performed to test the sufficient sparsity bound in actual DOT measurement scenario. In the phantom experiment, the experimental setup and procedures are similar to those used in [38]: The measurements are obtained from a container filled with 1% intralipid solution using a CW-based DOT imaging system (DYNOT, NIRx, New York). The optodes are placed on the top surface of the intralipid solution such that the tips of optodes just touch the liquid phantom surface, thus allowing no air gap between the tips and the liquid to minimize the refractive index (RI) mismatch. This setup provides us with a very similar boundary condition to that in light-tissue interaction situation. Thus, the experimental setup does not deviate too much from the traditional light-tissue interaction setup. The absorption and reduced scattering coefficients of the homogeneous background medium are $\mu_{a_0} = 0.08$ cm^{-1} and $\mu_{s_0} = 8.8$ cm^{-1}, respectively. The geometry of the probes is kept the same as that in the previous computer simulation, but the optodes here are bifurcated which means same optode can act as source and detector both. So effectively there are 25 sources and 25 detectors, and hence the sparsity bound is 25. The absorber is a square piece of size 1 cm by 1 cm having absorption coefficient around 0.052/cm placed at a depth of 2 cm below the surface of the liquid tissue phantom. The square is centered at the origin with respect to $X - Y$ plane and the thickness of the piece is 5 mm.

In the presented work, the reconstruction has been limited to two dimensions, since the main emphasis is on finding the 2-D support of the heterogeneity and it is assumed that the resolution in Z-direction is same as the thickness (around 5 mm) of the absorber. Hence a 2D image is reconstructed at a 2 cm depth making the 3D reconstruction problem a 2D slice reconstruction problem. Again $(Q1)$ is solved with different value of λ(giving different sparse solution) and keep the sparsest solution satisfying $||Ax - y||_2^2 < \sigma^2$. σ^2 is the noise variance estimated from the time samples of the measurements.

Following the above approach, the image is reconstructed using different resolution to verify the performance below and above the derived sparsity bound. The image resolution tested are 12×12, 24×24, 48×48 and 96×96 corresponding to voxel sizes of 5 mm by 5 mm, 2.5 mm by 2.5 mm, 1.25 mm by 1.25 mm and 0.625 mm by 0.625 mm, respectively. For these cases sparsity of the image is 4, 16, 64 and 256, respectively. So for the two lowest resolution images, sparsity is within the bound, i.e., 25, and the rest two high resolution images have sparsity above the sufficient limit. The reconstruction is shown in Fig. 3.5. The projection of the original absorber in 2D are shown as dash square. As it is visible from the reconstruction result, it is observed that for the lowest resolution, when the sparsity of the image $(= 4)$ is well below sufficient sparsity bound $(= 25)$, the support of the absorber is reconstructed correctly. For the next higher resolution though the sparsity $(= 16)$ is below the limit, the support is not recovered exactly, still the support is obtained with reasonable accuracy. For higher resolutions, when the sparsity of the image increases far above the sufficient sparsity limit, the reconstructed sparsest images tend to have much smaller support than the original image.

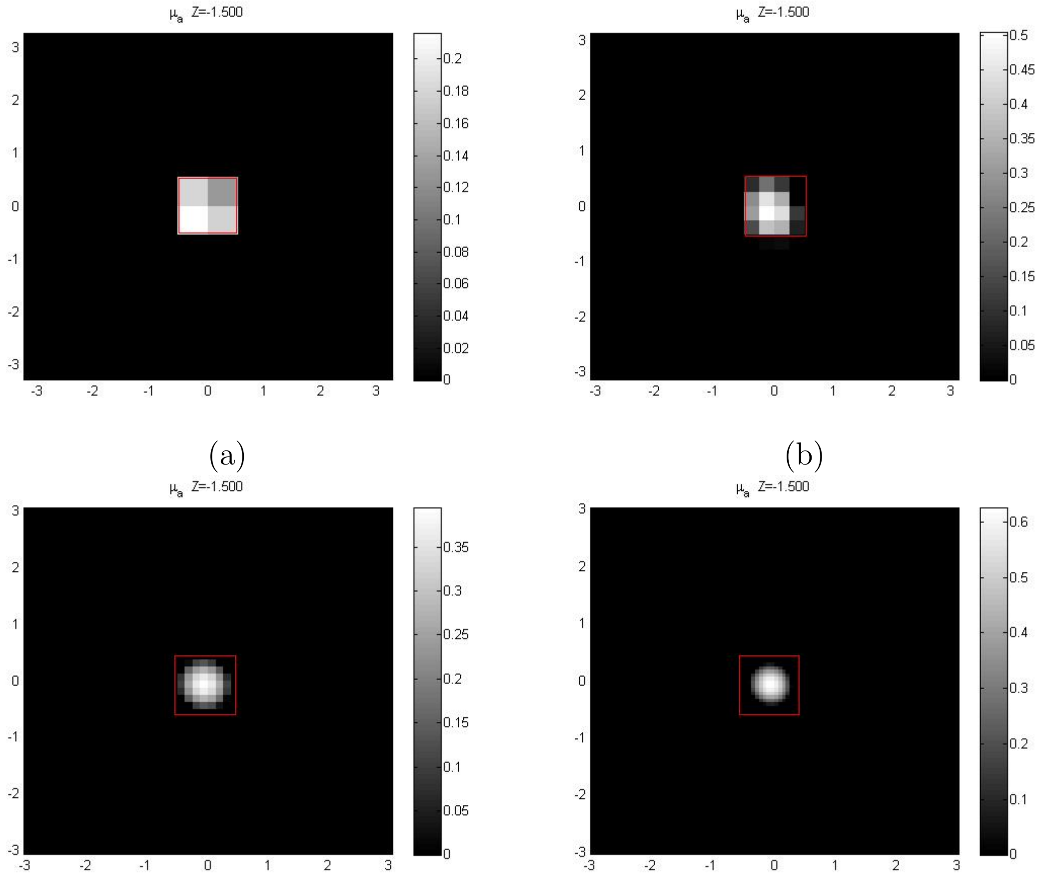

(a) (b)

(c) (d)

Figure 3.5. Reconstruction with different resolution and sparsity level using phantom experiment data (a) Resolution 12 by 12, Sparsity = 4; (b) Resolution 24 by 24, Sparsity = 16; (c) Resolution 48 by 48, Sparsity = 64; (d). Resolution 96 by 96, Sparsity = 256.

3.5 Conclusion

In this chapter the condition for the uniqueness of the solution of linear inverse scattering problem using Born and Rytov approximation is investigated. It is found that if the sparsity of the image is less than the average number of sources and detectors then the uniqueness of the sparse solution under Born and Rytov approximation is achieved in ideal scenario i.e. if one does not consider measurement noise and error due to linearization and discretization.

The Born and the Rytov reconstruction performance are analyzed for computer simulation and phantom experiment based data. Results show that reasonable reconstruction quality is achieved if the sparsity of the solution is within the sparsity bound derived for ideal case. Also the reconstruction quality degrades as one moves beyond the sparsity limit.

These results provide useful insight for setting the resolution of the medium to be imaged based on Born and Rytov approximation. By setting the resolution low, so that the sparsity is within the sufficient bound, one can ensure uniqueness of the sparse solution but at the same time discretization error should be taken care of. So finding the trade off between discretization error and reconstruction performance under Born/Rytov scheme can be a subject of future work. Although here one particular DOT application is discussed, the result derived in this paper will prove helpful for other imaging modality such as acoustic tomography and seismic imaging, where Born and Rytov approximation are used to solve the inverse scattering problem.

CHAPTER 4

DIMENSIONALITY REDUCED OPTIMIZATION

The computational cost of the ℓ_1 norm based optimization strategy to reach the sparse solution is very high for large number of voxels. Hence it is not suitable for real time application where the imaging volume is considerably large. Recently DOT, which is a special case of LISP, found widespread application in medical imaging [39, 40]. DOT reconstructs optical properties of a highly scattering medium in the near infra red (NIR) domain from the measurement of scattered and attenuated optical flux at the surface of the imaging volume. As the absorption of light in human tissues is low in the NIR region, NIR photons can penetrate several centimeters inside the tissue [33]. This makes DOT a promising tool in several biomedical imaging applications such as for brain imaging, breast and prostate cancer detection and molecular imaging [5, 29, 41]. Because of the nature of sparsity in DOT, sparsity regularization has been utilized to achieve high-quality DOT reconstruction. However, conventional approaches using sparse optimization are computationally expensive for 3-D DOT imaging of human tissues and have no selection criteria to optimize the regularization parameter. Hence it will be highly demanding to come up with a robust and computationally efficient algorithm for sparse 3D DOT reconstruction.

Conventional ℓ_1 optimization schemes involve solving a linear system with the size of unknown image which ensues the computational burden for large image size [19]. But for sparse images, if one can approximate the support of the nonzero voxels beforehead, then the size of linear system can be reduced drastically. Motivated by this insight , a novel algorithm, Dimensionality Reduction based Optimization for DOT (DRO-DOT), is developed. It reduces the dimensionality of the inverse DOT problem by reducing the number of unknowns in two steps and thereby makes the overall process fast. First, it constructs a low resolution voxel basis based on the sensing-matrix properties to find an image support. Second, it reconstructs the sparse image inside this support. To compensate for the reduced sensitivity with increasing depth, depth compensation is incorporated in DRO-DOT. An efficient method to optimally select the regularization parameter is proposed for obtaining a high-quality DOT image. DRO-DOT is also able to reconstruct high-resolution image even with a limited number of optodes in a spatially limited imaging set-up.

As discussed in chapter 2 in 4.15, either for Born or for Rytov approximation, in general, the linearized forward model for practical DOT measurement is $y = Ax + e$. Tikhonov regularization is widely used by DOT community to recover sparse DOT images by solving the inverse problem, because of its ease of implementation and computational speed [23, 27]. ℓ_2 regularized solution can be obtained in real time while suppressing high frequency noises. But the major drawback of Tikhonov approach is poor spatial resolution as the reconstructed image is over-smoothed or blurred [26]. Hence, it is difficult to reconstruct images which are sparse or have distinct boundary with respect to the background. As discussed in last section, sparseness of the optical heterogeneity is imposed by using the ℓ_1-norm regularization by solving the optimization problem $(Q1)$.[42] :

$$\hat{x} = \arg\min_{x} \{ \|Ax - y\|_2^2 + \lambda \|x\|_1 \} \tag{4.1}$$

With correct choice of λ, the ℓ_1 regularized solution $\hat{x}$ of equation 4.1 can accurately localize and quantify the absorption anomaly [26]. Researchers in DOT community have successfully used ℓ_1 regularization techniques to reconstruct sparse

DOT images [4, 26, 43, 44]. However, state of the art ℓ_1 norm minimization techniques involves solving a linear system with the size of the unknown image which ensues a huge computational burden for the full 3-D imaging volume [19, 20]. Hence the current ℓ_1-based approach is not suitable or practical for 3-D DOT reconstruction in real time.

A major challenge for the researchers in solving equation 4.1 is to select the correct regularization parameter. Although for Tikhonov regularization, well-researched theoretical guides exist to choose the parameter (γ) based on the l-curve and cross-validation method, for ℓ_1 optimization choosing the parameter λ is still an unsolved technical problem and the choice is made empirically [21, 12, 22].

The second challenge in DOT is that ℓ_1 or ℓ_2 regularized DOT reconstruction suffers from poor depth localization as the sensitivity of DOT measurement decreases exponentially along the depth [23, 24]. Pogue et al. proposed a spatially variant regularization scheme to enhance depth sensitivity [25]. Recently a more direct approach of modifying the sensing matrix to compensate for sensitivity decrease with increasing depth has been adopted [24, 26].

Another challenge for DOT research community is the optode geometry optimization, with which high quality reconstruction can be obtained by deploying a minimum number of optodes. Tian et al. have studied different optode configurations to find the optimal measurement density using ℓ_2-based regularization [27].

In this work, a novel reconstruction method is demonstrateed that is able to overcome the challenges mentioned so far for solving the sparse DOT inverse problem. For sparse images, the size of the linear system for the inverse problem can be reduced drastically if one can approximately create a low-resolution support mask of the nonzero voxels beforehand. Motivated by this insight, a two-step, dimensionality-reduction-based optimization (DRO) algorithm for DOT image reconstruction is developed. In the first step, DRO-DOT finds a low resolution support mask with potential nonzero voxels by identifying and grouping the sensing columns in A and the corresponding voxels of x. The number of such groups is far less than the number of original voxels. In the second and final step, ℓ_1 minimization is carried inside the recovered support mask only, whose size is smaller than the full 3-D imaging volume. Hence in both steps the number of unknowns is reduced, resulting from dimensionality reduction of the original problem and thereby scaling down the computational complexity. In addition, the sensing matrix A is re-weighted to enhance the depth sensitivity of the overall method by including depth compensation. The critical problem of chosing the regulariation parameter is also addressed by developing an adaptive scheme to find λ based on the statistical interpretation of ℓ_1 regularization in equation 4.1. By the end of this chapter, it is shown that, DRO-DOT is able to recover high-resolution images even with a limited number of optodes, which in turn reveals the possibility and feasibility of using transcretal DOT for prostate cancer imaging.

Overall, the major novelty of the approach is to solve an optimization model that consists of a data residue item and a sparse regularization item. The algorithm leads to three advantages: (1) It forms a low resolution supporting basis to reduce computing complexity. (2) It refines the depth compensation algorithm so as to recover more accurate DOT images. (3) It offers a semi-automatic method to choose optimal regularization parameter.

4.1 DRO-DOT

Consider a CW DOT imaging system, for which let the original image $x \in R^n$ represents the perturbation in absorption parameter, i.e., $x = [\delta\mu_a(r_1), \delta\mu_a(r_2), \ldots, \delta\mu_a(r_n)]^T$. Also x is sparse satisfying $\|x\|_0 << n$ and let I be the set of indices of the nonzero voxels, i.e. $I = \{i : x_i > 0\}$. Hence $\|x\|_0 = |I|$. Let I' be a subset of $\{1, 2, ..., n\}$

which contains the nonzero voxel locations i.e., $I \subset I' \subset \{1, 2, .., n\}$. If it is possible to approximate such a support I' so that $\|X\|_0 < |I'| = n' << n$, then the original forward problem of (4.15) can be re-stated as:

$$y = A_{I'} x_{I'}, \tag{4.2}$$

where $x_{I'}$ and $A_{I'}$ are the sub-vector and sub-matrix formed within voxels of x and columns of A chosen from the list I' respectively. Solving (4.2) is faster than solving the original problem (4.15), because now the dimensionality of the inverse problem is reduced to n' from n. This insight leads us to the first step of DRO-DOT.

4.1.1 Step-1

The original high-resolution 3-D voxel space is first transformed into a lower resolution voxel space and then the support of the heterogeneity is found in that space. Remember that A is the sensing matrix whose jth column corresponds to the measurement sensitivity in all the source-detector pairs for the jth voxel. Because of the diffusive nature of light propagation, the measurement sensitivity for x_j and x_k will be highly similar or correlated if these voxels are close. Thus the group of columns of A corresponding to the group of spatially close voxels should be highly correlated. This important rationale leads to the procedure for forming the low resolution voxel basis as follows: the algorithm starts from the first column of A i.e. A_1 and finds all columns that are highly correlated with A_1 (for example, setting a correlation coefficient threshold > 0.95). Then these correlated columns are grouped together as $A_1^\sharp$. The algorithm repeats the same process from the residual list of columns and continues the grouping process until A is fully exhausted. Let $n^\sharp$ groups are formed and each group is represented by the first column member of that group. The columns representing the jth group is denoted by $A_j^\sharp$. For each group of correlated columns, one needs to take the sum of the corresponding elements of x in that group (because of one-to-one correspondence between column locations and voxel positions) to form $x^\sharp$ which is the low resolution image basis of x such that, $x^\sharp_j$ = sum of elements of x corresponding to j th group of voxels. After forming this new basis, equation (4.15) can be approximated as:

$$y \approxeq \begin{bmatrix} A^\sharp_1 \dots A^\sharp_{n^\sharp} \end{bmatrix} \begin{bmatrix} x^\sharp_1 \\ \vdots \\ x^\sharp_{n^\sharp} \end{bmatrix} + e = A^\sharp x^\sharp + e \tag{4.3}$$

Choosing the correlation threshold is a crucial decision for performing the dimensionality reduction (from n to $n^\sharp$) in step-1. Suppose τ to be the correlation threshold. If τ is very high, there will be fewer number of columns in each group and hence $n^\sharp$ will be large and the benefit of dimensionality reduction will be lost. Again, if τ is very low, the approximation error $\|A^\sharp x^\sharp - Ax\|$ will be high. Hence it is important to find a trade-off between the approximation error and dimensionality reduction. The effective value of correlation threshold is chosen to be τ_e, such that the relative approximation error $\frac{\|A^\sharp x^\sharp - Ax\|}{\|Ax\|}$ remains less than 5% to ensure that one does not sacrifice accuracy in his pursuit to reduce computational burden. More details on how to select the effective correlation threshold τ_e are given in Section 1 of Supplementary Information.

Note that the collection of nonzero elements of $x^\sharp$ will correspond to the support for the sparse object only if the nonzero elements of x are of the same sign. Otherwise, a scenario is possible where the sum of nonzero voxels of different signs in some kth group is zero which will make $x^\sharp_k = 0$. Hence, to recover the support of the sparse object by finding nonzero elements of $x^\sharp$, it needs to be assured that the nonzero elements of x are of same sign, which in turn guarantees that if any kth group of voxels from x contains any number of nonzero elements, then $x^{\sharp}_{k} > 0$. Fortunately, for typical DOT imaging scenarios such as brain activation, presence of tumor etc., the change in absorption coefficient in the region of interest is known to be positive and researchers have used this non-negativity constraint to design their optimization strategies [45, 46]. With such positivity constraint on x, one can find this support by solving the modified version of equation 4.1 adapted to the new basis :

$$\hat{x^{\sharp}} = \underset{x^{\sharp}}{\arg\min}\{\|A^{\sharp}x^{\sharp} - y\|_2^2 + \lambda\|x^{\sharp}\|_1\} \tag{4.4}$$

This is the crucial step leading to the success of DRO-DOT. Equation 4.4 is solved using split augmented lagrangian shrinkage algorithm (SALSA) which is widely used for solving ℓ_1-minimization problem [19]. The convergence of SALSA for ℓ_1 regularization has been proven in section III B of Ref. [19]. In particular, the algorithm is said to converge when the relative change in the objective function falls below some pre-set tolerance limit. In appendix C, convergence of DRO-DOT is illustrated.

4.1.2 Step-2

After finding the low resolution voxel basis, this basis is mapped back to the original voxel basis to get I' as discussed before. ℓ_1 minimization is then performed inside this support I' instead of the full imaging volume. Therefore one needs to solve the new optimization problem associated with equation (4.2):

$$\hat{x_{I'}} = \underset{x_{I'}}{\arg\min}\{\|A_{I'}x_{I'} - y\|_2^2 + \lambda\|x_{I'}\|_1\} \tag{4.5}$$

As the number of voxels in I' is n', which is much smaller than n, the optimization problem in equation 4.5 is computationally inexpensive.

4.2 Depth Compensation

As the measurement sensitivity degrades exponentially along the depth of the tissue, reconstructed image becomes biased towards the surface. This problem of poor depth localization is addressed earlier by post-multiplication of the A matrix and spatially varying regularization approach [25, 24]. In the current work, the first approach is followed with modification. For $n = n_x \times n_y \times n_z$, A can be re-written as concatenation of n_z block matrices corresponding to n_z layers:

$$A = \begin{bmatrix} A_1 | A_2 | \ldots A_{n_z} \end{bmatrix} \tag{4.6}$$

In principle, sensitivity of A_i should be bigger than sensitivity of A_j if $i < j$. To equalize or compensate for this sensitivity attenuation along the depth, each block of A is reweighted as follows [26]:

$$\mathring{A} = AM \qquad where \qquad M = \begin{bmatrix} \theta(A_{n_z}) & & & \\ & \ddots & & \\ & & \theta(A_2) & \\ & & & \theta(A_1) \end{bmatrix} \tag{4.7}$$

where $\theta(A_i)$ is the maximum singular value of ith block. Thus the sensitivity for the last layer is boosted most and for the first layer it is suppressed most. Now one can obtain a depth localized image by solving the modified optimization problem of equation 4.1 as follows:

$$\hat{\mathring{x}} = \arg\min_{\mathring{x}} \{ \| \mathring{A}\mathring{x} - y \|_2^2 + \lambda \| \mathring{x} \|_1 \} \tag{4.8}$$

One more step is required to find the final optimized solution $\hat{x}$ from $\hat{\mathring{x}}$ as :

$$\hat{x} = M^{-1} \hat{\mathring{x}} \tag{4.9}$$

Equation (4.9) preserves the quantification of the reconstructed image after depth equalization.

4.3 Selection of regularization parameter

It is known that the success of ℓ_1 regularization depends on the correct selection of regularization parameter λ. To avoid biasing of the reconstruction result, this choice should not be based on a trial-and-error approach [22]; rather, an automatic selection criterion is required. In this research, a semi-automatic method of choosing λ is proposed for the standard DOT experimental paradigms. The method is based on statistical interpretation of the regularization parameter as a ratio of measurement noise level and sparsity parameter. It can be shown that the solution of equation 4.1 is indeed the maximum a posteriori (MAP) estimator for the linear model (4.15) with a Laplacian prior and Gaussian noise model, as given below:

$$p(y|x) = \frac{1}{\sigma\sqrt{2\pi}} e^{-\frac{\|y - Ax\|_2^2}{2\sigma^2}} \tag{4.10}$$

$$p(x) = \frac{1}{2\alpha} e^{-\frac{\|x\|_1}{\alpha}} \tag{4.11}$$

where σ^2 is the measurement noise variance and α is the sparsity parameter. The MAP estimator can be found by maximizing the joint probability which results in the following convex optimization:

$$x_{MAP} = \arg\min_x \{\|y - Ax\|_2^2 + 2\frac{\sigma^2}{\alpha}\|x\|_1\} \tag{4.12}$$

Comparing (4.12) with equation 4.1 readily gives:

$$\lambda = 2\frac{\sigma^2}{\alpha} \tag{4.13}$$

In general, one does neither know the noise variance nor the sparsity of the original image in advance. Hence making the right choice for λ requires trying different combination of these two independent parameters and it is not known which one is the right combination. It is possible to have a good estimate of the noise variance σ^2 from adequate number of time samples of DOT measurements, owing to the excellent sampling rate and thus temporal resolution of DOT. Also the range of α can be estimated based on clinical/biomedical knowledge and estimation. As an example, for prostate or breast cancer, even though the tumor location, shape and severity are unknown, one would expect only a few suspicious lesions, namely, to have a few sparse objects to be imaged and found. Knowing a realistic range, the sparsity parameter α can be estimated. This range can be discretized as $\{\alpha_1, \alpha_2, \ldots, \alpha_l\}$, where α_1 and α_l corresponds to the minimum and maximum possible value of the sparsity parameter. This gives a range of λ values where $\lambda_i = 2\frac{\sigma^2}{\lambda_i}$. The appropriate λ can be chosen from that range based on the discrepancy principle [47]. According to the discrepancy principle the correct choice of λ will make the data discrepancy equal to the noise variance. Hence the optimum λ denoted by $\hat{\lambda}$ is chosen such that,

$$\hat{\lambda} = \arg\min_{\lambda_i}\{|\frac{1}{mq}\|Ax_{\lambda_i} - y\|_2^2 - \sigma^2|\} \tag{4.14}$$

$$where\ \ \lambda_i \in \{2\sigma^2/\alpha_i\}_{i=1}^{n} \qquad for\ \ i = \{1, 2, \ldots, l\}$$

Where x_{λ_i} is the solution for ℓ_1 regularization with $\lambda = \lambda_i$. The practical utility of this method is of utmost importance to reconstruct tissue properties in real time without any assistance from other imaging modalities.

4.4 Frequency Domain DOT

While solving the DOT inverse problem for the linear model described by $y = Ax + e$, it is assumed until now that x is absorption parameter and y is continuous wave (CW) light measurement. For many of the DOT imaging applications such as brain imaging, it is sufficient to recover only the absorption coefficient variation $\delta\mu_a$ assuming that the scattering coefficient μ_s' is nearly constant. But in case of prostate DOT imaging, several recent studies have reported that light scattering of prostate cancer is significantly different from normal prostate tissue [48, 49]. Thus perturbation in the scattering coefficient $\delta\mu_s'$, can be used to distinguish malign tumor from the normal tissue. Hence, the ability to accurately recover $\delta\mu_s'$ along with $\delta\mu_a$ is essential if one wishes to apply DOT for early prostate cancer detection using a transrectal prostate DOT setup. In the CW system, only the signal intensity can be measured, which does not allow one to distinguish the effects of light absorption from scattering [50, 51]. A Frequency Domain (FD) system measures the amplitude and phase shift of the either transmitted or reflected photon density waves from the tissue [48]. Detection of both amplitude and phase shift facilitates quantification and imaging of $\delta\mu_a$ and $\delta\mu_s'$ simultaneously.

For FD DOT, linear system of equation 4.15 is modified as :

$$y_{FD} = A_{FD}x_{FD} + e \tag{4.15}$$

where $y_{FD} = [real(y) \quad imag(y)]^T \in R^{2mq\times 1}$, $x_{FD} = [x_{\delta\mu_a} \quad x_{\delta\mu_s'}]^T \in R^{2n\times 1}$. Because the measurement now has both amplitude and phase, hence y_{FD} is complex where the first half is the real part and second half is the imaginary part. The first half of x_{FD} is the absorption parameter and second half is scattering parameter at n voxels and hence $x_{FD} \in R^{2n\times 1}$. With this formulation for the FD DOT problem, DRO-DOT can be applied to reconstruct x_{FD} from the FD measurement y_{FD}.

4.5 Performance Metrics

Four parameters are used to evaluate the quality of reconstruction with DRO-DOT:

Area Ratio (AR): This quality metric is defined as the area ratio between the reconstructed object and original object for 2D image [27]:

$$AR = \frac{A_r}{A_t} \tag{4.16}$$

where A_r and A_t are the area of reconstructed and true object in 2D, respectively. A_r is calculated using the full width half maximum (FWHM) approach.

Volume Ratio (VR): For 3D reconstruction, a more relevant evaluation metric is volume ratio (VR), as introduced:

$$VR = \frac{V_r}{V_t} \tag{4.17}$$

where V_r and V_t are the volume of reconstructed and true object in 3D, respectively. V_r is also calculated using FWHM in 3 dimensions.

Contrast Ratio (CR): CR is defined as the ratio of the mean value of reconstruction in the region of interest(ROI) i.e., inside the true object boundary and mean value of the background (BG) outside the object boundary, as given by:

$$CR = \frac{mean(x_{ROI})}{mean(x_{BG})} \tag{4.18}$$

As x represents the change in absorption coefficient, ideally $x = 0$ in the background and hence for perfect reconstruction, $CR \rightarrow \infty$.

Run Time (RT): RT is the total time taken by the reconstruction algorithm to complete the computation process, assuming the regularization parameter is already selected.

4.6 Results

4.6.1 Performance Evaluation

The accuracy of newly developed DRO-DOT algorithm has to be evaluated in terms of localization and quantification of reconstructed object. Also the computational efficiency needs to be independently evaluated. To establish or demonstrate the superiority of DRO-DOT, DRO-DOT is compared with two other state of the art optimization techniques extensively used for DOT reconstruction. The first one is Tikhonov regularization and second one is the conventional ℓ_1 regularization used for sparse object recovery. The experimental set-up is illustrated in Figure 4.1. This laboratory phantom experiment is designed to mimic the brain imaging paradigm, where 5×5 optodes with a minimum optode separation of 1 cm are arranged on the surface. The 25 optodes are bifurcated, permitting each of them to transmit and detect the NIR light through the tissue phantom. A black cylindrical disk of 1.1cm in diameter and 0.4cm in thickness is placed into the 1% intralipid phantom, with one circular side facing up. The depth of the center of the absorbing object is 1.5cm and it is located along the center of the $x - y$ plane. For more details about the set-up and instrumentation, the reader can refer to the work of Tian et. al. [27].

As described in the Method step-1 section, after plotting the relative approximation error $\frac{\|A^\sharp x^\sharp - Ax\|}{\|Ax\|}$ for different values of correlation threshold, it is observed that the relative error goes below 5% for $\tau \geq 0.96$. Hence $\tau_e = 0.96$ is set, which reduces the dimensionality by more than 80% in step-1. The tolerance limit for convergence of the ℓ_1 regularized optimization is set to be 10^{-5}, namely, the calculation stops when the relative difference in the cost function becomes lower than 10^{-5}. $\lambda = 0.0251$ is found by applying the novel regularization parameter selection approach.

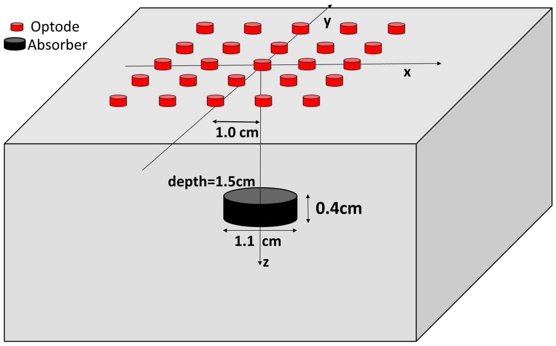

Figure 4.1. Schematic diagram of the experimental setup. The optode array is a 5×5 geometry of bifurcated source-detector optodes with a 1cm separation between neighboring optodes. A cylindrical absorption anomaly is placed into the intralipid phantom along the center of the grid at a depth of 1.5cm below the surface..

Fig. 4.2 depicts the two-step reconstruction of the object at sequential layers for the phantom experiment shown in Fig. 4.1. It is known that the sensitivity pattern for each source-detector pair follows a banana shape, and outside of that shape objects are not detectable [52]. Hence the imaging volume for reconstruction is taken to be $4cm \times 4cm \times 2.5cm$. Initial visual inspection of the reconstruction clearly shows that DRO-DOT recovers the image location in 3D and size with good accuracy and high contrast [Fig. 4.2a]. And it is important to note that owing to the novel regularization parameter selection approach, the reconstruction is done without any prior information on the true size and location of the object. At the same time the computational complexity is greatly reduced: Step-1 took 1.9s and Step-2 took just 0.17s to achieve convergence. Given that this is 3D reconstruction, the time taken is much shorter than conventional ℓ_1 based methods. This shows the promise by DRO-DOT for real time functional DOT imaging applications. At this point, it is warranted to have a fair comparison between DRO-DOT and other state of the art DOT recovery algorithms.

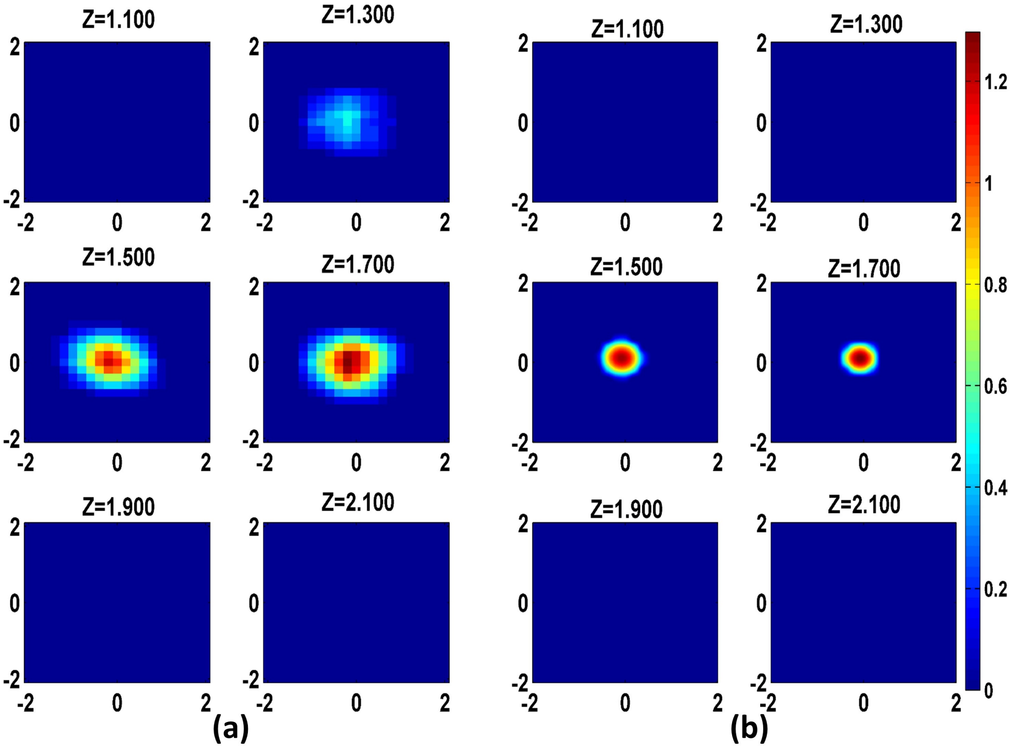

Figure 4.2. DRO-DOT step by step reconstruction for the tissue phantom: (a) The low resolution image support region recovered in Step-1 and (b) The final reconstructed image obtained in Step-2 by solving ℓ_1 optimization inside the support region obtained in Step-1..

DRO-DOT is compared to two other conventional methods that are extensively used for DOT reconstruction: ℓ_2 norm and ℓ_1 norm based optimization respectively. Fig. 4.3 shows the image reconstruction at a plane of depth 1.5cm from the surface (along the centre of the object). As can be seen, both DRO-DOT and ℓ_1 based method outperform ℓ_2 minimization approach in terms of image localization and quantization. ℓ_2 minimization is fast, easy to solve and has the automated regularization parameter selection such as $l-curve$ and Generalized Cross Validation method [47, 22]. But it suffers from over-smoothing effect as shown in Fig. 4.3a. ℓ_1 minimization promotes sparseness and hence good quality reconstruction, but the computational burden is very high for a large number of voxels which is indeed a challenge for 3D DOT reconstruction. Also the choice of regularization parameter in ℓ_1 based approach is heuristic which needs prior information of image size and location. It is claimed that DRO-DOT gives at least as good quality as ℓ_1 minimization while using a small amount of computational time without any prior information to find an optimal regularization parameter.

At this point, a quantitative comparison between DRO-DOT and the state of the art techniques should be carried out in terms of different quality metrics following the common practice [26, 27]. Table 4.1 compares the performance of DRO-DOT with other two optimization schemes in terms of reconstruction quality and speed. It shows that AR and VR values are close to unity by DRO-DOT and pure ℓ_1 method, whereas these values are greater than 1 by ℓ_2 regularization because of the over-smoothing effect. DRO-DOT and the ℓ_1 method also offer approximately 4 times better contrast than the ℓ_2 method. The run time of DRO-DOT is as short as that of the ℓ_2 method and 5 times faster than the pure ℓ_1 method. Thus DRO-DOT achieves best of the both aspects: enhanced quality of ℓ_1 reconstruction and high speed of ℓ_2 optimization.

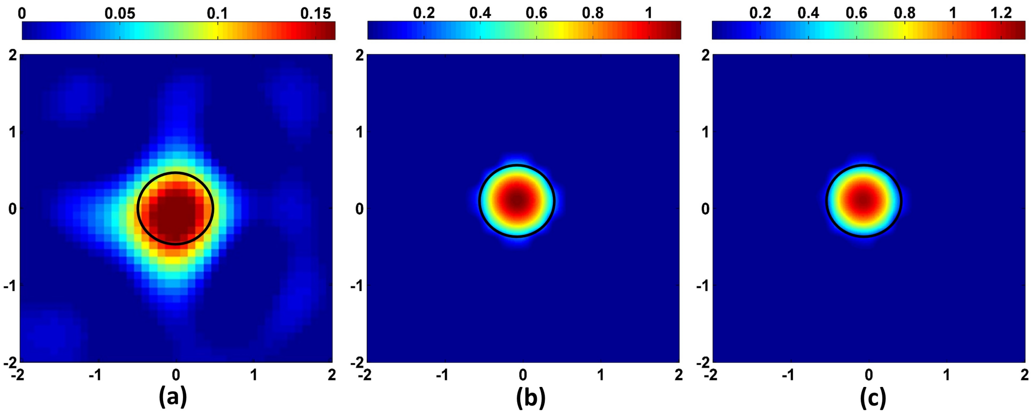

Figure 4.3. Reconstruction at Z=1.5cm plane for (a) ℓ_2-norm minimization method (b) ℓ_1-norm minimization method and (c) DRO-DOT. The black circle represents the perimeter of the true object in each case. .

Table 4.1. Comparison of DRO-DOT with pure ℓ_1 and ℓ_2 based methods

	DRO-DOT	ℓ_1-minimization	ℓ_2-minimization
AR	0.98	0.97	1.13
VR	0.97	1.05	1.24
CR	87.25	86.38	17.90
RT(s)	2.61	13.55	2.73

4.6.2 Depth Compensation

The sensitivity of the measurement wanes rapidly with increasing depth. Hence the reconstruction is bound to be biased near the surface. By incorporating depth compensation (DC) in DRO-DOT, i.e., truthfully reconstructing the deeper layers more than the near surface layers, it is possible to reconstruct a DOT image at correct depth. Fig. 4.4 shows how depth compensation mitigates the depth-biasing effect. The reconstruction with and without depth compensation is shown along the two vertical planes $y-z$ and $x-z$. It can be seen that without DC, the reconstruction comes near the surface and the depth of the object center is wrongly biased at 1.1cm. With DC the center is reconstructed at 1.6cm depth which is close to the original (1.5cm).

4.6.3 Optode Placement

In Fig. 4.1, the set up is with a dense array of 25 bifurcated source and detectors. Such a setting can be afforded in cases where a wide open area is available for multiple optode placements such as for brain imaging and breast cancer detection. However, in some clinical applications where a very limited space is available to place an adequate number of optodes, such as transcretal imaging for prostate cancer detection, DOT

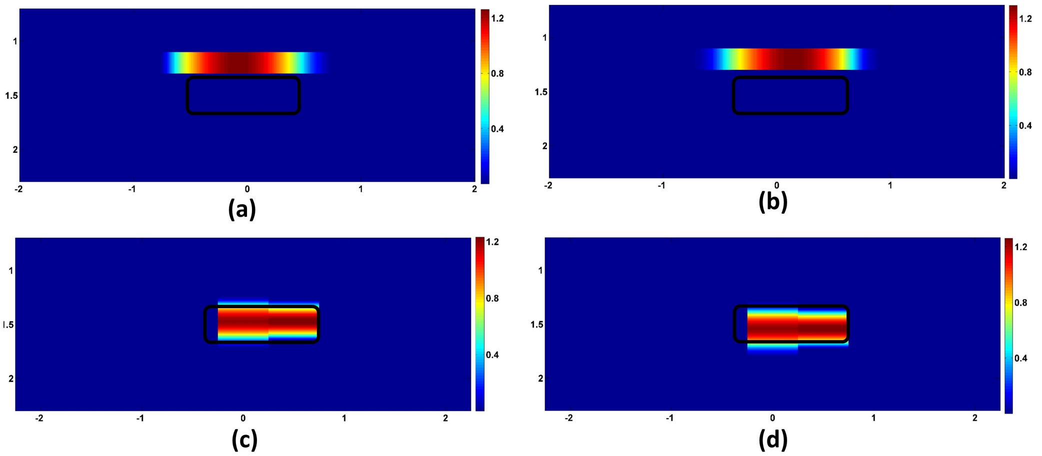

(a) (b)

(c) (d)

Figure 4.4. Reconstruction along the vertical planes with and without DC. The first row shows reconstruction without DC along (a) $y - z$ plane (b) $x - z$ plane. Reconstruction with DC is in the second row (c) $y - z$ plane (d) $x - z$ plane. The original object outline is shown in black..

will face a major challenge in order to achieve high-resolution image [53]. Even in case of functional brain imaging, lengthy set-up time needed for many optodes adds to subject's discomfort [27]. But decreasing the number of optodes or measurements makes the DOT image reconstruction more ill-posed and thus the reconstruction quality is bound to suffer. Hence it is interesting and important to know how much one can afford to decrease number of optodes without degrading image quality. Such a study had been done earlier by Tian et. al. [27], but the reconstruction method used is based on ℓ_2 minimization, and hence in general, it suffered from the oversmoothing effect. As DRO-DOT is already ℓ_1 based and therefore promotes sparsity, in general, it is expected to achieve better quality DOT reconstruction for all different geometries.

Fig. 4.5 lists four different source detector geometries to be evaluated for comparison. They are named as geometry SD-I, SD-II, SD-III and SD-IV. SD-I is the same geometry being used in the phantom experiment [Fig. 4.1] and results in reconstructed DOT images shown in Figs. 4.2 - 4.4 . SD-II is also 5×5 optode geometry similar to SD-I, with sources and detectors placed alternately (i.e. no bifurcation). SD-III and SD-IV are derived from SD-I by discarding one row and three rows of optodes, respectively, also without bifurcation. For SD-II to SD-IV, the data sets of measurements are selected or reduced from the original measurements in SD-I.

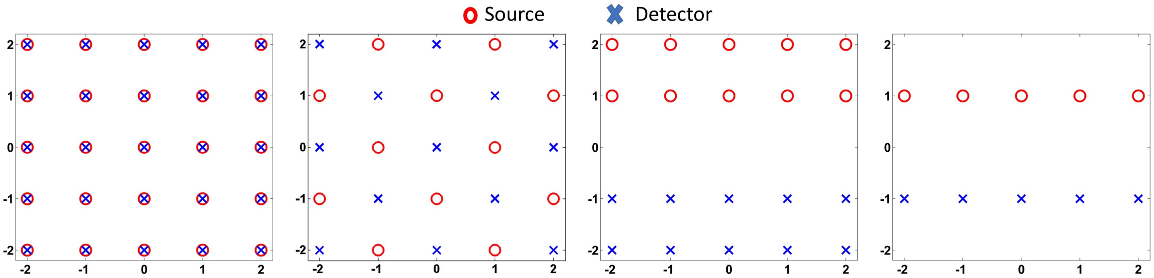

(a) (b) (c) (d)

Figure 4.5. Different optode geometries (a) SD-I (b) SD-II (c) SD-III (d) SD-IV. .

Fig. 4.6 shows the reconstruction for the four different optode geometries at the center of the object i.e., at the depth of 1.5cm. It can be seen that the reconstructed image size and location are recovered almost exactly for each case, except for some difference in quantification.

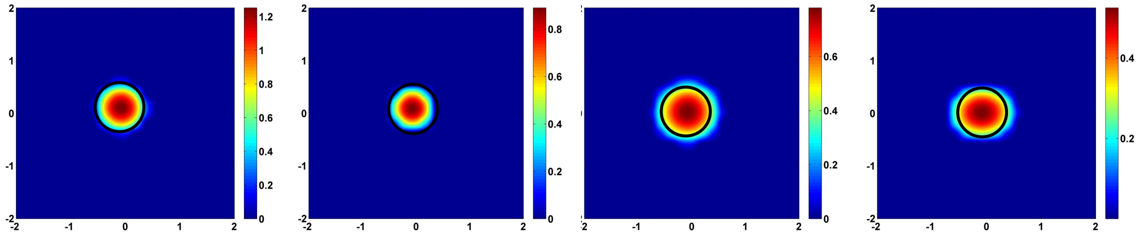

(a) (b) (c) (d)

Figure 4.6. Reconstruction using DRO-DOT at $x - y$ plane at depth 1.5cm for (a) SD-I (b) SD-II (c) SD-III (d) SD-IV. .

In addition, Table D.1 shows that using DRO-DOT, the quality of the reconstruction is maintained high even with a very limited number of sources and detectors used.

Table 4.2. Comparison of DRO-DOT reconstruction for different optode geometries

	SD-I	SD-II	SD-III	SD-IV
VR	0.97	0.92	1.02	1.02
CR	87.25	67.26	47.90	45.10

4.6.4 Transcretal Prostate Imaging

In the previous section, it has been demonstrated that even when there are two rows of optodes, DRO-DOT is able to localize the object at the correct depth and position with a high contrast. This observation leads us to focus on a challenging application of DOT: transcretal prostate cancer imaging. In prostate imaging, the optode probe has to be inserted through the subject's anus where a very limited space is available for optode placement and only two rows of closely placed optodes can be used [53]. To investigate the feasibility of DRO-DOT for transcretal imaging, several laboratory experiments are carried out with the optode set-up shown in Fig. 4.7. Nine sources and nine detectors are placed alternately in two rows making a total number of 81 measurements. The two rows are separated by 2cm and the closest optode separation is 0.5cm. The homogeneous background is 1% intralipid solution, giving the background absorption coefficient of $\simeq 0.03cm^{-1}$.

Four different phantom configurations as shown in Fig. 4.7 with objects of different shapes and sizes are used to evaluate 3D image reconstruction using DRO-DOT. Object B is a spherical ball with $\simeq$ 0.9cm diameter. Cs is a much smaller object

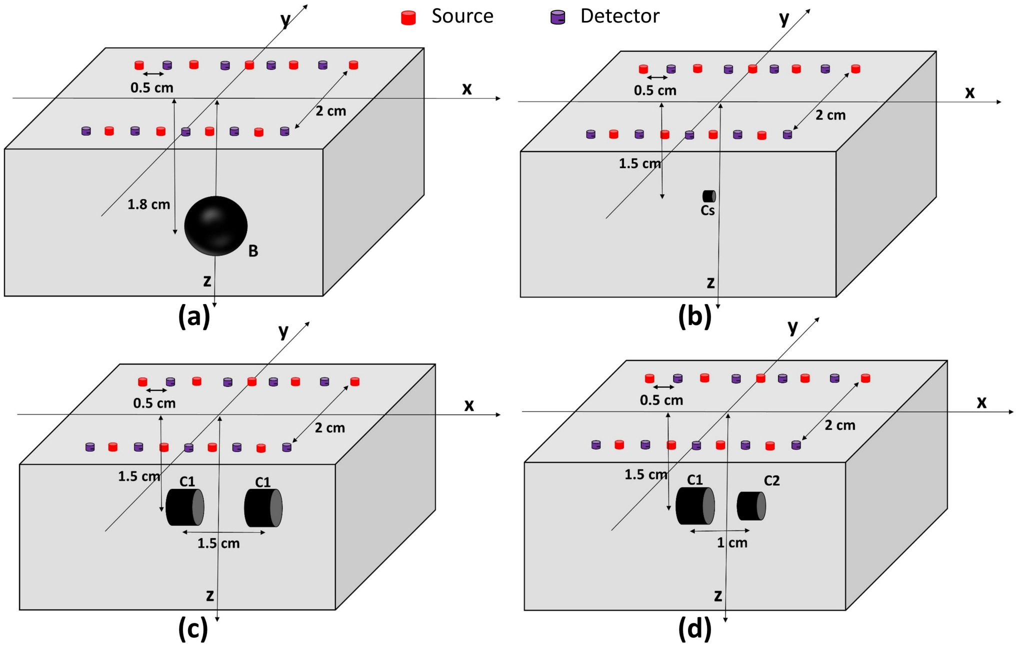

Figure 4.7. Experimental set-up for different phantom configurations (a) single object of type B placed at a depth of 1.8cm (b) single tiny object of type Cs placed at a depth of 1.5cm (c) dual identical objects of type $C1$ placed at 1.5cm depth with center to center separation of 1.5cm (d) dual objects of two different types $C1$ and $C2$ placed at 1.5cm depth with center to center separation of 1cm. .

of cylindrical shape with a diameter of $\simeq 0.2$cm and a length of $\simeq 0.3$cm. Object $C1$ is a cylinder with a diameter of $\simeq 0.85$cm and a length of $\simeq 0.62$cm. Object $C2$ is also a cylinder but with diameter of $\simeq 0.65$cm and a length of $\simeq 0.45$cm. In the first experiment, B is placed at a depth of 1.8 cm (Fig. 4.7a). The second experiment is more challenging as it needed to reconstruct a tiny object Cs that is placed at a depth of 1.5 cm (Fig. 4.7b). The other two experiments are also interesting as those needed to reconstruct dual objects. In one case, two $C1$ objects are placed at 1.5cm depth and are separated by 1.5cm center-to-center distance making the separation between their close surfaces around 0.8-0.9cm (Fig. 4.7b). In the fourth experiment, two cylinders with different sizes i.e., $C1$ and $C2$ are closely spaced with a 1cm center-to-center distance or 0.45cm surface-to-surface distance at 1.5cm depth (Fig. 4.7c). The imaging volume used in DRO-DOT is chosen to be $6cm \times 4cm \times 2.5cm$ right below the optode surface.

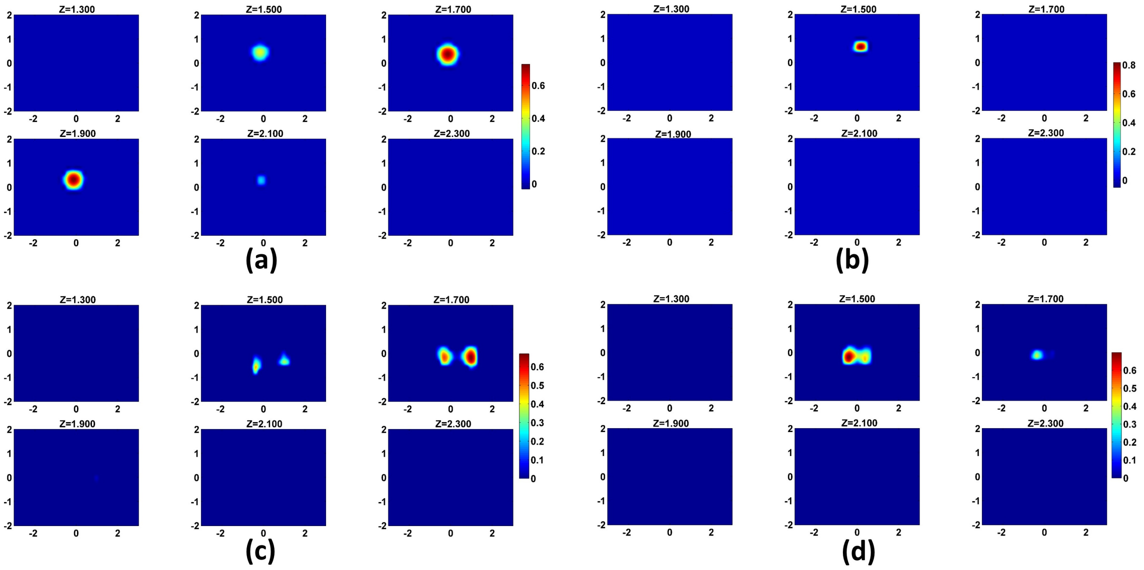

Figure 4.8. Reconstructed DOT images from four different DOT phantom experiments using transcretal geometry (a) Set-up 1: Object B placed at 1.8cm depth, (b) Set-up 2: Object Cs placed at 1.5cm depth (c) Set-up 3: Two identical cylindrical objects of both $C1$ separated by a 1.5 cm center-to center distance at 1.5cm depth and (d) Set-up 4: Two different sized objects $C1$ and $C2$ with a 1cm center-to-center separation at 1.5cm depth. .

Fig. 4.8a shows the reconstructed image using DRO-DOT for the ball-shaped object. The size and location of the spherical object is recovered accurately. Fig. 4.8b shows the ability of DRO-DOT to reconstruct an object of dimension as low as 0.2cm. For the first dual-object phantom experiment, two $C1$ objects are resolved with good accuracy as seen in Fig. 4.8c. For the second dual-object case with one $C1$ and one $C2$ object, the reconstruction is shown in Fig. 4.8d. In this case, though the two objects are distinguishable, there no more exists a clear boundary between them.

This experiment demonstrates that DRO-DOT can not separate objects separated less than 5mm.

4.7 FD-DOT Reconstruction

A frequency domain DOT system is simulated using PMI toolbox. Two different scenarios are studied for the experiment. In first case a pure absorption and a pure scattering anomaly are placed at different locations. In second case, they are at the same position meaning the same object both absorbs and scatters the light. The true object boundary is shown in black circle. The optode geometry is same as shown in Fig. 4.7. The value of $\delta\mu_a = 0.03$ and $\delta\mu_s' = 3$ is chosen for the anomaly. Also 1% noise is added to the measurement to simulate the noisy measurement scenario. It was not possible to perform FD measurement in the laboratory, but in future when the system will be available, DRO-DOT can be verified with real phantom experiment FD data. The reconnstruction results in 4.9 shows that the object is localized with almost accurate quantification.

4.8 Conclusion

A novel algorithm to rapidly reconstruct high quality 3D DOT image is developed which can be potentially used in real time in future. The novelty of the algorithm rests on the formation of a low resolution supporting basis in its first step by grouping highly correlated columns within the sensing matrix. This step enables one to solve the inverse problem using ℓ_1-minimization with a small number of low resolution voxels so as to find the approximate image support. Traditionally any prior information from other imaging modalities, such as magnetic resonance imaging(MRI), positron emission tomography(PET) or ultrasound (US) is always useful to

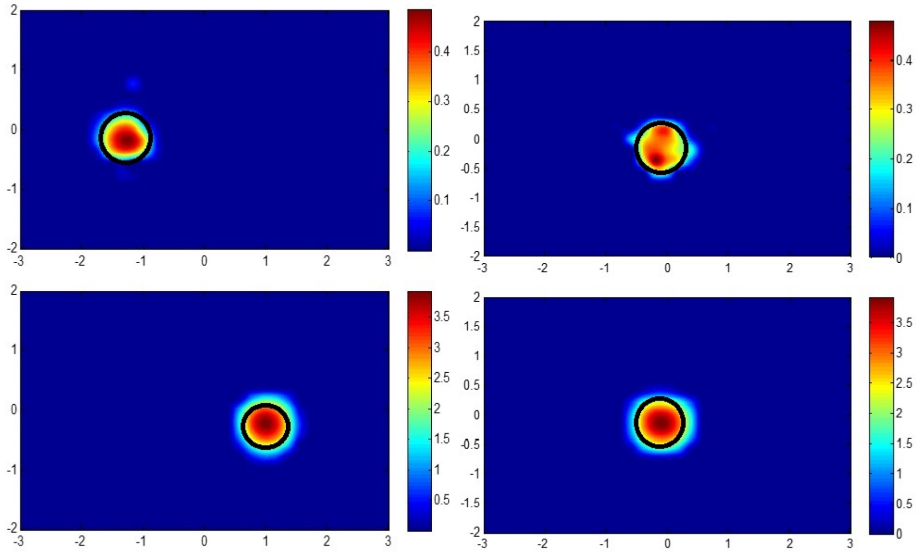

(a) (b)

Figure 4.9. Simultaneous reconstruction of both absorption and scattering parameter with absorber and acatterer at (a)different positions and (b)same position. Top figure corresponds to reconstruction of $\delta\mu_a$ and bottom figure shows reconstruction of $\delta\mu_s'$.

provide additional mathematical and/or anatomical constraints that ultimately lead to higher quality reconstructed images [41, 53, 54]. In general, however, acquisition of multi-modality images is not always feasible and adds burden on healthcare costs. The first step of DRO-DOT effectively addresses this issue by being able to recover the image support without any prior information. Within this low-resolution support, the true object can be found in a very short time in the second step using ℓ_1 optimization. Thus DRO-DOT algorithm achieves the superior quality of ℓ_1 optimization and at the same time remains computationally inexpensive.

The experimental validation of DRO-DOT to examine the quality and speed of image reconstruction has been performed using standard laboratory phantom experiments. Reconstructed images using DRO-DOT are compared with those by state of the art ℓ_1 and ℓ_2 based optimization techniques. The reconstructed image quality is quantified by such metrics as AR, VR, and CR. Also, computational complexity for each algorithm is judged by comparing their respective runtimes. Table 4.1 shows that both the new method and ℓ_1 perform excellently leading to high-quality reconstructed images, whereas ℓ_2 minimization does not offer recovered images with high spatial resolution and contrast. This result is expected because the final step of DRO-DOT actually runs ℓ_1 minimization inside the support basis found from the first step, which in principle gives rise to an improved spatial resolution compared to images obtained by ℓ_2 minimization. The total runtime for DRO-DOT and ℓ_2 minimization is found to be around 80% less than the runtime of ℓ_1 method. The improved computational speed in DRO-DOT stems from the fact that the computational burden of ℓ_1 optimization for the huge number of voxels in the 3D imaging volume is reduced by breaking the process into two steps. Both of the steps actually reduce the dimensionality of the original larger sensing matrix and hence reduce the computational burden. In this way, DRO-DOT has achieved an optimal aspect of two existing state of the art ℓ_1 and ℓ_2 based optimization techniques, i.e., high solution quality of ℓ_1 optimization and high speed of ℓ_2 optimization.

The problem of depth localization has also been addressed in the present work. The sensing matrix A is modified by assigning more weights to the deeper layers of A forming $\mathring{A}$ using equation (4.7). As shown in Fig. 4.4, this approach reveals the details in deeper layers and preserves the correct depth in the reconstruction, in contrast to the poor depth localization without depth compensation. It should be acknowledged that a similar depth compensation method is earlier used by Kavuri et. al. [26], though they did not do the correction step as described by equation (4.9). While this step requires only multiplication of the post-processed image $\mathring{x}^*$ by the inverse diagonal weight matrix M^{-1} to reach x^*, it is very important for recovering accurate quantification of the imaged object. An earlier study reports that quantification of absorption perturbation can be recovered with a best rate of

64 % in simulative experiments for reconsructed images [55]; current approach with equation (4.9) permits much improved recovery rate of 99.1%.

As DRO-DOT requires utilization of ℓ_1 minimization to solve the inverse problem internally, choosing the correct or appropriate regularization parameter λ is a major challenge. This challenge is addressed by developing an efficient scheme to choose λ based on the statistical interpretation of its dependence on noise variance and the discrepancy principle. This simplification is possible specifically for DOT scenario because σ^2 can be estimated accurately from multiple data collections of the measurements. Then, DRO-DOT is able to systematically select an optimal regularization parameter λ without time and effort consuming, subjective search of such a parameter.

The study has also clearly demonstrated that DRO-DOT can achieve good-quality DOT image reconstruction even with a limited number of optodes. Fig. 4.6 shows that one can optimize the optode setting geometry, namely, reduce the total number of optodes, without significantly sacrificing the image quality. Although reducing the number of optodes makes the inverse problem (i.e. image reconstruction) more ill-posed and underdetermined, proposed method compensates for this ill-posedness by reducing the dimensionality of the problem. DRO-DOT is still able to achieve excellent VR and CR (Table D.1) after the source-detector pairs are reduced from 25 × 25 to 5 × 5 (Fig. 4.5). This result is an excellent improvement compared to the previously known results [27].

Based on the observation that DRO-DOT works well even with limited space to place adequate optodes, its application has been extended to prostate cancer imaging. The real imaging scenario is emulated using laboratory phantom experiments specially designed for this purpose, namely, having a transcretal optode setting (Fig. 4.7). DRO-DOT is able to reconstruct single and dual objects with accurate localization and high CR. The reconstruction algorithm can not separate two small objects if their separation is less than 5mm. Early research has shown that the spatial resolution in DOT can not be less than 5mm [29]. Hence the proposed algorithm has achieved the highest possible spatial resolution. It is worth to compare the current work with the reports by Xu et al. and Kavuri et al. on prostate DOT studies [41, 53]. Their methods are based on ℓ_2 regularization and for 3D imaging, they are computationally expensive as both of the methods uses NIRFAST software package to do the forward and backward calculation using finite element method at each iteration [56]. In contrast, DRO-DOT uses ℓ_1 regularization and is very fast or computationally inexpensive.

Although the results by DRO-DOT are promising for DOT imaging with improved resolution and computational speed, a few weaknesses of this study are to be recognized and possibly improved in the near future. For DRO-DOT to perform well, the object to be imaged should be both sparse and localized. Such constraint is needed for $x^\sharp$ to be sparse in the low dimensional voxel space (equation 4.3), which in turn guarantees the success of solving equation 4.4. For example, if the nonzero voxels of x are randomly scattered, then $x^\sharp$ will have an equal number of nonzero regions in x, and hence the dimensionality reduction of the support basis cannot be achieved through step-1. Fortunately, such cases with multi focal lesions are not too common in practice, and most of the time there are not more than two focci for us to focus on [57]. Another limitation is the inability to simultaneously reconstruct absorption and scattering perturbation with the current setup and corresponding algorithm.

In conclusion, a novel method DRO-DOT, for 3D DOT reconstruction has been developed and experimentally supported. It can rapidly reconstruct high-quality images in very short time. The proposed method does not require prior information from other imaging modalities and thus holds promise for cost reduction and patient convenience, while keeping high quality of image reconstruction. DRO-DOT also incorporates procedures for accurate depth localization and systematic/automatic selection of regularization parameter. As a specific example, several experimental tissue phantom measurements with transcretal imaging geometry are taken, and the optimal performance of DRO-DOT in respective imaging scenarios has been demonstrated. Overall, DRO-DOT provides a new platform for rapid high-resolution DOT imaging ready for clinical translation in medical imaging applications.

CHAPTER 5

SUMMARY AND FUTURE WORKS

5.1 Summary

The major contributions of this dissertation are to establish the sparse recovery condition for linear inverse scattering problem and development of a rapid and high quality image reconstruction algorithm.

In the first part of this work, uniqueness condition for obtaining the sparsest solution of LISP is derived. Born and Rytov approximation is re-formulated as MMV problem and hence it is argued that the condition for obtaining the unique sparsest solution of MMV problem applies to them. Based on few realistic assumptions, it is found that the sparse solution for the Born and Rytov LISP is the unique sparsest one if the sparsity level is less than the average number of sources and detectors. Computer simulation and phantom experiment results validate this uniqueness condition.

A rapid and high quality image reconstruction algorithm DRO-DOT is developed to solve the sparse signal recovery problem arising in DOT, which is a particular instance of LISP useful for medical diagnostics. The algorithm reduces the dimensionality of the original inverse problem in two steps, thereby making the overall optimization computationally efficient. Previously developed depth compensation method is incorporated in the algorithm with minor corrections, to account for the reduction in measurement sensitivity with increasing depth. A semi-automatic method of regularization parameter selection is developed based on the statistical interpretation of the sparsity regularization. Based on the observation that DRO-DOT works well even with limited space to place adequate optodes, its application has been extended to prostate cancer imaging. Overall, DRO-DOT provides a new platform for rapid high-resolution DOT imaging ready for clinical translation in medical imaging applications. Further evaluation of this method with animal tissues ex vivo and/or in vivo as well as human experiment will enhance and better validate the algorithm.

5.2 Future Directions

5.2.1 Real-time medical imaging

In Ch. 4, DRO-DOT was applied for laboratory phantom experiments. Evaluating the performance with real human experiment data will be next step. If it is possible to adapt DRO-DOT for practical DOT measurements, this algorithm may further be applied to enhance the speed of functional brain imaging reconstruction. One might also want to explore the scope of applying the algorithm for other application specific inverse scattering problems. Further evaluation of the method with animal tissues ex vivo and/or in vivo as well as human experiment will enhance and better validate our algorithm.

5.2.2 Noise normalization

The ℓ_1 optimization problems $(Q1)$ or $(Q1')$ being solved in this work are based on the assumption of white gaussian noise(WGN) present in the data. But in practical medical or seismic scenarios this assumption may no longer be valid. For example, in DOT measurement signal to noise ratio (SNR) decreases with separation between source and detector [58] and [59]. Thus a noise normalization approach should be incorporated in the proposed algorithm based on the characteristic of measurement noise.

APPENDIX A

Acronyms

3-D	Three-Dimensional
AR	Area Ratio
CR	Contrast Ratio
CS	Compressive Sensing
CW	Continuous-Wave
DOT	Diffuse Optical Tomography
DRO-DOT	Dimensionality Reduction based Optimization for Diffuse Optical Tomography
FD	Frequency Domain
ISP	Inverse Scattering Problem
LISP	Linear Inverse Scattering Problem
MAP	Maximum A Posteriori
MRI	Magnetic Resonance Imaging
MMV	Multiple Measurement Vector
NIR	Near Infra Red
PDF	Probability Distribution Function
ROI	Region Of Interest
RT	Run Time
SALSA	Split Augmented Lagrangian Shrinkage Algorithm
SD	Source-Detector
SNR	Signal-to-Noise Ratio
VR	Volume Ratio
WGN	White Gaussian Noise

APPENDIX B

Setting the Correlation Threshold

The effective correlation threshold τ_e was set to ensure that the relative approximation error $||\frac{||A^\sharp x^\sharp - Ax||}{||Ax||}$ remains below 5%. For each of the DOT geometries studied in the paper, a set of 100 random test images were generated. For each of this random test images, we calculated the relative approximation error, $E(i)$ for $i = \{1, 2, \ldots, 100\}$, as a function of correlation threshold τ. By the end of this process, we obtained 100 values of $E(i)$ for each value of τ and then averaged them to generate a single value of average relative approximation error, E_a for each value of τ. Finally, the effective correlation threshold τ_e was decided from the plot of average relative approximation error E_a vs correlation threshold τ by finding the point where E_a goes below 5%. Supplementary Fig. B.1a shows such a plot for the DOT geometry of Fig. 1 in the paper. We also plot the dimensionality reduction factor $r = \frac{n - n^\sharp}{n}$ as a function of τ in Fig. B.1b.

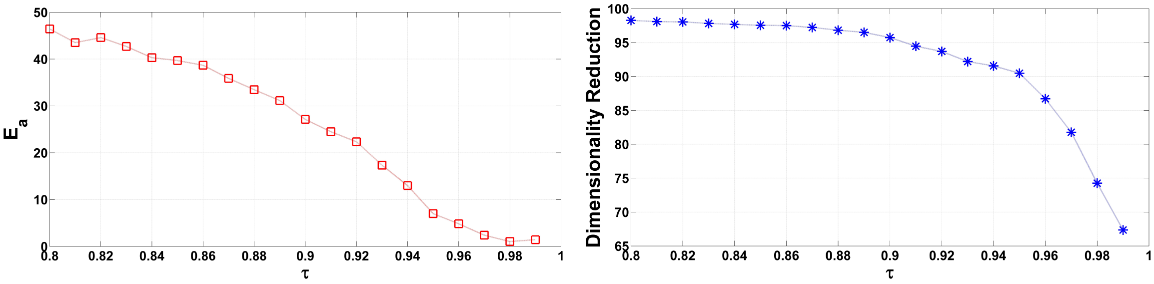

(a) **(b)**

Figure B.1. Setting of τ_e in Step-1 and its effect on dimensionality reduction for the geometry of Fig. 1 in the thesis. (a) Plot of average relative approximation error E_a vs correlation threshold τ and (b) Plot of % dimensionality reduction factor r vs correlation threshold τ. We set $\tau_e = 0.96$ as the effective correlation threshold where E_a goes below 5%. For the chosen value of τ_e, a reduction of dimensionality (or number of columns of A matrix) as much as 85% was achieved in step-1 of DRO-DOT .

APPENDIX C

Convergence of SALSA

The evolution of the cost function with time is plotted in Fig. C.1 to illustrate the convergence of DRO-DOT. The convergence is shown for the phantom experiment in Fig. 1.

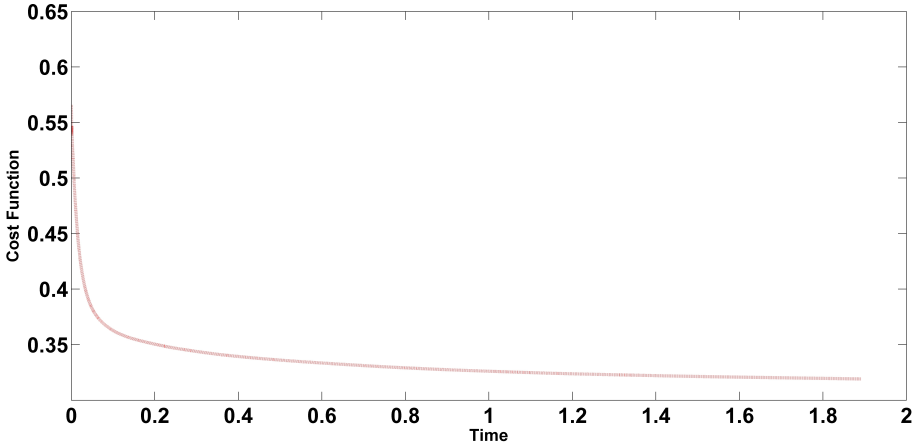

Figure C.1. Convergence of SALSA in DRO-DOT step-1 for the phantom experiment in Fig. 1 of paper. The plot shows the evolution of the ℓ_1 regularized objective function with successive iteration time. SALSA coverges at $\simeq 1.9s$ i.e. at that time the relative error in the cost function betwen two successive iterations goes below our tolerance limit that we set as 10^{-5}.

APPENDIX D

Experimental Parameters

DRO-DOT algorithm has been applied for five different experimental set-ups: Four optode geometries for the brain imaging phantom study (Fig. 5) and one optode geometry for transcretal prostate phantom experiment (Fig. 7). In the table below we show the different parameters related to each of these experiment set-up:

Table D.1. Parameters for different phantom experiments. Geometry 1-4 are for brain imaging phantom with different optode configuration as in Fig. 5 of the paper. Geometry 5 is for the transcretal prostate phantom whose geometry is shown in Fig. 7.

	Effetive Correlation Threshold (τ_e)	dimensionality reduction (%) r=$\frac{n-n^\sharp}{n}$	λ	Time to converge (seconds) (step-1 & step-2)
Geometry 1	0.96	85	0.0251	1.90 & 0.17
Geometry 2	0.95	88	0.0346	1.82 & 0.15
Geometry 3	0.95	87	0.0371	1.85 & 0.16
Geometry 4	0.97	81	0.0441	2.28 & 0.22
Geometry5	0.96	85	0.0282	1.98 & 0.18

REFERENCES

[1] S. Gerritsen. *Waves in inhomogeneous media.* Ph. D. Thesis, Delft University of Technology, Delft, The Netherlands, 2007.

[2] A. J. Devaney. Inversion formula for inverse scattering within the born approximation. *Opt. Lett.*, 7(3):111–112, 1982.

[3] T. J. Cui, W. C. Chew, A. A. Aydiner, and S. Chen. Inverse scattering of two-dimensional dielectric objects buried in a lossy earth using the distorted born iterative method. *IEEE Trans. Geosci. Remote Sens.*, 39(2):339–346, 2001.

[4] T. Durduran, R. Choe, W. Baker, and A. G. Yodh. Diffuse optics for tissue monitoring and tomography. *Rep. Prog. Phys.*, 73(7):076701, 2010.

[5] M. A. O'Leary. *Imaging with diffuse photon density waves.* PhD thesis, University of Pennsylvania, United States – Pennsylvania, 1996. Ph.D.

[6] N. Joachimowicz, C. Pichot, and J. P. Hugonin. Inverse scattering: An iterative numerical method for electromagnetic imaging. *IEEE Trans. Antennas Propag.*, 39(12):1742–1753, 1991.

[7] F. C. Lin and M. A. Fiddy. The born-rytov controversy: I. comparing analytical and approximate expressions for the one-dimensional deterministic case. *J. Opt. Soc. Am. A*, 9(7):1102–1110, 1992.

[8] M. Slaney and A. Kak. Principles of computerized tomographic imaging. *SIAM, Philadelphia*, 1988.

[9] A. Tikhonov. Solution of incorrectly formulated problems and the regularization method. In *Soviet Math. Doklady*, volume 4, pages 1035–1038, 1963.

[10] P. C. Hansen. Analysis of discrete ill-posed problems by means of the l-curve. *SIAM Review*, 34(4):561–580, December 1992.

[11] Kim. S. J., K. Koh, M. Lustig, S. Boyd, and D. Gorinevsky. An Interior-Point method for Large-Scale l1-Regularized least squares. *IEEE J. Sel. Topics Signal Process.*, 1(4):606–617, December 2007.

[12] R. Tibshirani. Regression shrinkage and selection via the lasso. *J. R. Stat. Soc. Ser. B Stat. Methodol.*, 58(1):267–288, January 1996.

[13] M. Lustig, D. L. Donoho, J. M. Santos, and J. M. Pauly. Compressed sensing MRI. *IEEE Signal Process. Mag.*, 25(2):72–82, March 2008.

[14] O. K. Lee, J. M. Kim, Y. Bresler, and J. C. Ye. Compressive diffuse optical tomography: noniterative exact reconstruction using joint sparsity. *IEEE Trans. Med. Imag.*, 30(5):1129–1142, 2011.

[15] M. E. Davies and Y. C. Eldar. Rank awareness in joint sparse recovery. *IEEE Trans. Inf. Theory*, 58(2):1135–1146, 2012.

[16] M. Lustig, D. Donoho, and J. M. Pauly. Sparse MRI: the application of compressed sensing for rapid MR imaging. *MAGNET. RESON. MED.*, 58(6):1182–1195, October 2007.

[17] E. J. Candes and M. B. Wakin. An introduction to compressive sampling. *IEEE Signal Process. Mag.*, 25(2):21–30, November 2008.

[18] J. Chen and X. Huo. Theoretical results on sparse representations of multiple-measurement vectors. *IEEE Trans. Signal Process.*, 54(12):4634–4643, 2006.

[19] M.V. Afonso, J.M. Bioucas-Dias, and M.A.T. Figueiredo. An augmented lagrangian approach to the constrained optimization formulation of imaging inverse problems. *IEEE Trans. Image Process.*, 20(3):681–695, 2011.

[20] A. Beck and M. Teboulle. A fast iterative shrinkage-thresholding algorithm for linear inverse problems. *SIAM J, Imaging Sci.*, 2(1):183–202, 2009.

[21] P. C. Hansen. Analysis of discrete Ill-Posed problems by means of the L-Curve. *SIAM Review*, 34(4):561–580, December 1992.

[22] Christina Habermehl, Jens Steinbrink, Klaus-Robert Müller, and Stefan Haufe. Optimizing the regularization for image reconstruction of cerebral diffuse optical tomography. *J. Biomed. Opt.*, 19(9):096006, 2014.

[23] D. A. Boas, A. M. Dale, and M. A. Franceschini. Diffuse optical imaging of brain activation: approaches to optimizing image sensitivity, resolution, and accuracy. *NeuroImage*, 23(Supplement 1):S275–S288, September 2004.

[24] H. Niu, Z. J. Lin, F. Tian, S. Dhamne, and H. Liu. Comprehensive investigation of three-dimensional diffuse optical tomography with depth compensation algorithm. *J. Biomed. Opt.*, 15(4):046005–046005, 2010.

[25] B. W. Pogue et. al. Spatially variant regularization improves diffuse optical tomography. *Appl. Opt.*, 38(13):2950–2961, 1999.

[26] V. C. Kavuri, Z. J. Lin, F. Tian, and H. Liu. Sparsity enhanced spatial resolution and depth localization in diffuse optical tomography. *Biomed. Opt. Express*, 3(5):943–957, 2012.

[27] F. Tian, G. Alexandrakis, and H. Liu. Optimization of probe geometry for diffuse optical brain imaging based on measurement density and distribution. *Appl. Opt.*, 48(13):2496–2504, 2009.

[28] W. B. Beydoun and A. Tarantola. First born and rytov approximations: Modeling and inversion conditions in a canonical example. *J. Acoust. Soc. Am.*, 83:1045, 1988.

[29] V. Ntziachristos. *Concurrent diffuse optical tomography, spectroscopy and magnetic resonance imaging of breast cancer*. PhD thesis, University of Pennsylvania, United States – Pennsylvania, 1996. Ph.D.

[30] D. L. Donoho. For most large underdetermined systems of linear equations the minimal l1-norm solution is also the sparsest solution. *Comm. Pure Appl. Math.*, 59(6):797–829, 2006.

[31] D. L. Donoho and M. Elad. Optimally sparse representation in general (nonorthogonal) dictionaries via l1 minimization. *Proc. Natl. Acad. Sci. U.S.A.*, 100(5):2197–2202, 2003.

[32] Josselin Garnier and Knut Solna. Passive imaging and detection in cluttered media. In *Computational Advances in Multi-Sensor Adaptive Processing (CAMSAP), 2009 3rd IEEE International Workshop on*, pages 225–228. IEEE, 2009.

[33] C. L. Tsai, J. C. Chen, and W. J. Wang. Near-infrared absorption property of biological soft tissue constituents. *J. Med. Biol. Eng.*, 21(1):7–14, 2001.

[34] D. Boas et. al. Photon migration imaging (pmi) toolbox. *http://www.nmr.mgh.harvard.edu/PMI/resources/toolbox.htm*, 2004.

[35] S. R. Arridge and M. Schweiger. Photon-measurement density functions. part 2: Finite-element-method calculations. *Appl. Opt.*, 34(34):8026–8037, 1995.

[36] W. F. Cheong, S. A. Prahl, and A. J. Welch. A review of the optical properties of biological tissues. *IEEE J. Quantum Electron.*, 26(12):2166–2185, December 1990.

[37] E. Van Den Berg and M. P. Friedlander. Spgl1: A solver for large-scale sparse reconstruction. *http://www. cs. ubc. ca/labs/scl/spgl1*, 2007.

[38] H. Niu, F. Tian, Z. J. Lin, and H. Liu. Development of a compensation algorithm for accurate depth localization in diffuse optical tomography. *Opt. Lett.*, 35(3):429–431, February 2010.

[39] N. Cao, A. Nehorai, and M. Jacobs. Image reconstruction for diffuse optical tomography using sparsity regularization and expectation-maximization algorithm. *Opt. Express*, 15(21):13695–13708, October 2007.

[40] O. K. Lee, Jong M. K., Y. Bresler, and J. C. Ye. Compressive diffuse optical tomography: Noniterative exact reconstruction using joint sparsity. *IEEE Trans. Med. Imag.*, 30(5):1129–1142, May 2011.

[41] D. Piao et. al. Alternative transrectal prostate imaging: a diffuse optical tomography method. *IEEE J. Sel. Topics Quantum Electron.*, 16(4):715–729, 2010.

[42] N. Cao, A. Nehorai, and M. Jacobs. Image reconstruction for diffuse optical tomography using sparsity regularization and expectation-maximization algorithm. *Opt. Express*, 15(21):13695–13708, 2007.

[43] M. Szen, A. Giannoula, and T. Durduran. Compressed sensing in diffuse optical tomography. *Opt. Express*, 18(23):23676–23690, November 2010.

[44] C. B. Shaw and P. K. Yalavarthy. Prior image-constrained l1-norm-based reconstruction method for effective usage of structural information in diffuse optical tomography. *Opt. lett.*, 37(20):4353–4355, 2012.

[45] F. Larusson, S. Fantini, and E. L. Miller. Hyperspectral image reconstruction for diffuse optical tomography. *Biomed. Opt. Express*, 2(4):946–965, 2011.

[46] M. A. OLeary, D. A. Boas, B. Chance, and A. G. Yodh. Experimental images of heterogeneous turbid media by frequency-domain diffusing-photon tomography. *Opt. lett.*, 20(5):426–428, 1995.

[47] C. R. Vogel. *Computational methods for inverse problems*, volume 23. Siam, 2002.

[48] T. Svensson, MargrÃt EinarsdÃ̀gttÃr, K. Svanberg, and S. Andersson-Engels. In vivo optical characterization of human prostate tissue using near-infrared time-resolved spectroscopy. *J. Biomed. Opt.*, 12(1):014022–014022, 2007.

[49] V. Sharma et. al. Prostate cancer detection using combined auto-fluorescence and light reflectance spectroscopy: ex vivo study of human prostates. *Biomed. Opt. Express*, 5(5):1512–1529, 2014.

[50] S. R. Arridge and W. R. B. Lionheart. Nonuniqueness in diffusion-based optical tomography. *Opt. Lett.*, 23(11):882–884, 1998.

[51] M. A. OLeary, D. A. Boas, B. Chance, and A. G. Yodh. Experimental images of heterogeneous turbid media by frequency-domain diffusing-photon tomography. *Opt. Lett.*, 20(5):426–428, 1995.

[52] S. B. Colak et. al. Tomographic image reconstruction from optical projections in light-diffusing media. *Appl. Opt.*, 36(1):180–213, 1997.

[53] V. C. Kavuri and H. Liu. Hierarchical clustering method to improve transrectal ultrasound-guided diffuse optical tomography for prostate cancer imaging. *Acad. Radiol.*, 21(2):250–262, 2014.

[54] X. Intes, C. Maloux, M. Guven, B. Yazici, and B. Chance. Diffuse optical tomography with physiological and spatial a priori constraints. *Phys. Med. Biol.*, 49(12):N155, 2004.

[55] F. Tian, H. Niu, S. Khadka, Z. J. Lin, and H. Liu. Algorithmic depth compensation improves quantification and noise suppression in functional diffuse optical tomography. *Biomed. Opt. Express*, 1(2):441–452, 2010.

[56] H. Dehghani et. al. Near infrared optical tomography using nirfast: Algorithm for numerical model and image reconstruction. *COMMUN. NUMER. METH. EN.*, 25(6):711–732, 2009.

[57] M. Andreoiu and L. Cheng. Multifocal prostate cancer: biologic, prognostic, and therapeutic implications. *Hum. Pathol.*, 41(6):781–793, 2010.

[58] R. Gaudette et. al. A comparison study of linear reconstruction techniques for diffuse optical tomographic imaging of absorption coefficient. *Phys. Med. Biol.*, 45(4):1051, April 2000.

[59] P. K. Yalavarthy, B. W. Pogue, H. Dehghani, and K. D. Paulsen. Weight-matrix structured regularization provides optimal generalized least-squares estimate in diffuse optical tomography. *Med. Phys.*, 34(6):2085–2098, June 2007.

BIOGRAPHICAL STATEMENT

Tanmoy Bhowmik was born in Agartala, India, in 1984. He received his B.Tech. degree in Electronics and Communication Engineering from Motilal Nehru National Institute of Technology, India, in 2006. From 2006 to 2010, he worked in ST Microelectronics as digital design engineer. He started his MS in Electrical Engineering at University of Texas at Arlington in 2010 and in 2011 he started as a direct PhD track student. His current research interest is in the area of inverse problem in medical imaging.